remote sensing

MDPI

Review

Martian Dust Storms: Reviews and Perspective for the Tianwen-3 Mars Sample Return Mission

Fei He [1,2,*], Zhaojin Rong [1,2], Zhaopeng Wu [1], Jiawei Gao [1,2], Kai Fan [1], Xu Zhou [1], Limei Yan [1,2], Yuqi Wang [1] and Yong Wei [1,2]

[1] Key Laboratory of Earth and Planetary Physics, Institute of Geology and Geophysics, Chinese Academy of Sciences, Beijing 100029, China; rongzhaojin@mail.iggcas.ac.cn (Z.R.); wuzp@mail.iggcas.ac.cn (Z.W.); gaojw@mail.iggcas.ac.cn (J.G.); kaif@mail.iggcas.ac.cn (K.F.); zx0601@mail.iggcas.ac.cn (X.Z.); lmyan@mail.iggcas.ac.cn (L.Y.); wangyq@mail.iggcas.ac.cn (Y.W.); weiy@mail.iggcas.ac.cn (Y.W.)

[2] College of Earth and Planetary Sciences, University of Chinese Academy of Sciences, Beijing 100049, China

* Correspondence: hefei@mail.iggcas.ac.cn

Abstract: Dust storms play a crucial role in the climate system and the space environment of Mars, significantly impacting human exploration activities on the planet. The Martian dust storms exhibit significant regional, seasonal and interannual variations due to various controlling factors such as large-scale atmospheric circulation, varying solar radiation forcing, and Martial orbital and rotational motions and their coupling to the atmospheric dynamics. This paper aims to review current understandings of Martian dust storms. This paper begins by elucidating the basic properties of dust storms, their driving mechanisms, and their impacts on atmospheric dynamics, atmospheric electric property, space environment, topography, and Mars explorations. The paper then introduces the observation methods on different platforms, including orbiters and landers/rovers, along with datasets constructed based on these historical observations of Martian dust storms. Finally, we propose dust storm monitoring and predicting for the upcoming Chinese Tianwen-3 Mars sample return mission. It concludes by depicting the future research topics aimed at systematically understanding Martian dust storms.

Keywords: Mars; dust storm; remote sensing; monitor and prediction; tianwen-3 mission

check for updates

Citation: He, F.; Rong, Z.; Wu, Z.; Gao, J.; Fan, K.; Zhou, X.; Yan, L.; Wang, Y.; Wei, Y. Martian Dust Storms: Reviews and Perspective for the Tianwen-3 Mars Sample Return Mission. *Remote Sens.* **2024**, *16*, 2613. https://doi.org/10.3390/rs16142613

Academic Editor: Roberto Orosei

Received: 24 June 2024
Revised: 14 July 2024
Accepted: 16 July 2024
Published: 17 July 2024

1. Introduction

Mars is the fourth terrestrial planet and the second smallest planet in the solar system after Mercury. It is known as the "Red Planet" due to its surface being covered with hematite. The radius of Mars is 3390 km, significantly smaller than Earth. The aphelion and perihelion of the Mars orbit are 1.666 AU ($1\ \text{AU} \approx 1.5 \times 10^8$ km) and 1.381 AU, respectively, with an eccentricity of 0.933941 and a sidereal orbital period of 686.98 Earth days. Mars lacks a global dipolar magnetic field [1] and has lost most of its atmosphere to space over billions of years [2]. Presently, Mars is frigid and arid because most of its water has escaped through various processes influenced by several factors [3–9], such as solar wind variations, solar extreme ultraviolet (EUV) radiations, and dust storms.

The lack of a protective global dipolar magnetic field leads to persistent escape of the Martian atmosphere, resulting in an extremely thin and cold atmosphere with surface atmospheric pressure only reaching 0.6% that of Earth's. Dominated by carbon dioxide (95.3%) [10], the Martian atmosphere undergoes significant seasonal variations due to the large difference between the aphelion and perihelion of Mars orbit, which generates clear seasonal variations in climate and environment. The seasonal cycle on Mars results in changes in surface atmospheric pressure by up to 20% due to sublimation and condensation of carbon dioxide in polar regions [11]. Additionally, the high eccentricity of Mars' orbit causes dramatic variation in solar radiation, fluctuating by as much as 30% during a Martian year (MY) [12]. Various textbooks, e.g. [10,13,14] and reviews, e.g. [15,16], offer detailed insights into satellite observations and understanding of the Martian atmosphere.

Mars' surface features include river channels, canyons, ravines, and alluvial plains. Research suggests that Mars may have been habitable around 3 billion years ago, with a global dipole magnetic field, abundant liquid water, and a dense atmosphere [17]. This history makes Mars a focal point for human planetary exploration driven by the search for extraterrestrial life. Over fifty missions, including orbiters, landers, and rovers, have significantly advanced our understanding of Mars' environment [18,19]. Surface missions face challenges due to Martian environmental factors. Among Mars' seasonal variations, dust storms are particularly prominent and significantly influence Martian climate, surface conditions, space environment, and atmospheric escape [20]. Dust storms have become the biggest threat to missions landing on the surface of Mars.

Extensive reviews on Martian dust storms, e.g. [21–25], provide valuable insights. This paper focuses on summarizing current knowledge of Martian dust storms in order to guide China's Tianwen-3 Mars sample return mission. It aims to offer comprehensive information for scientific researchers and mission planners, focusing on dust storm properties, driving mechanisms, impacts, detection principles and methods. Section 2 introduces basic dust storm properties, reviews driving mechanisms, and summarizes impacts on Mars' surface and space environment. Section 3 covers the history of observing dust storms on Mars and outlines observation principles and methods (including orbiters and landers/rovers). Section 4 includes statistical predictions of dust activity for Tianwen-3 and discusses our proposed dust storm monitoring scheme, which was officially accepted for the mission. Concluding remarks are provided in Section 5.

2. Martian Dust Storms

Dust storms on Mars are the most dramatic activity in its climate system, involving both the surface and atmosphere, and exhibit significant seasonal variations. Each Martian year, particularly as Mars approaches its southern summer solstice, local, regional, and sometimes global dust storms (Figure 1) become highly active. In this section, we will review the fundamental properties of dust storms and their impacts on the Martian environment.

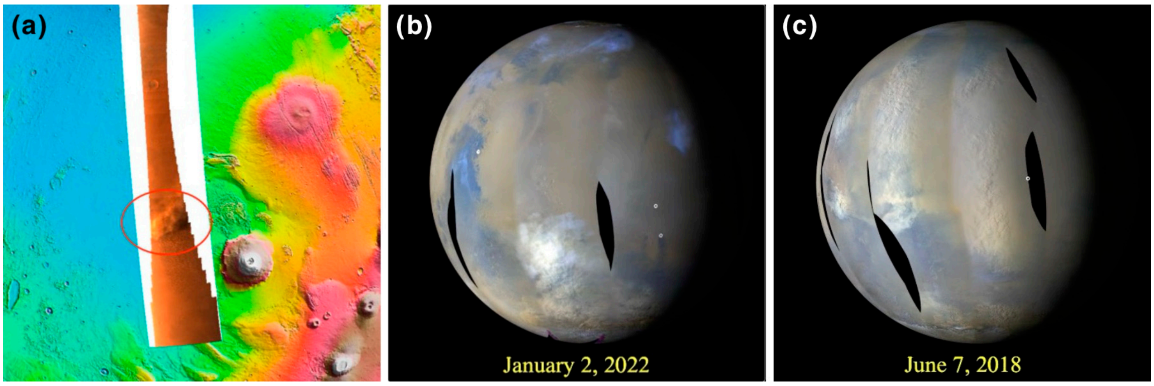

Figure 1. Illustrations of local, regional, and global dust storms. (**a**) A local dust storm in the Amazonis Planitia near Olympus Mountain was captured by the Moderate Resolution Imaging Camera (MoRIC) onboard the Tianwen-1 mission on 6 January 2022. The red circle denotes the local dust storm. (**b**) A regional dust storm in the southern hemisphere was captured by the Mars Color Imager (MARCI) onboard Mars Reconnaissance Orbiter (MRO) [26]. (**c**) A global dust storm in 2018 was captured by the MARCI onboard MRO [27].

2.1. Basic Properties of Dust Storms

Martian dust storms can be categorized based on different criteria. According to their scales, they are classified as local dust storms, regional dust storms, and global dust storms [22,28], as depicted in Figure 1. A regional dust storm is defined by dust events covering an area $\geq 1.6 \times 10^6$ km^2 and lasting longer than 2 days. Dust lofted during these events can travel significant distances, sometimes encircling Mars within a latitude zone and settling far from its source region. Smaller or shorter-duration events are classified as local dust storms, typically lasting less than 3 days. Global dust storms, known as planet-encircling dust storms, sweep the entire Martian globe. These storms rapidly expand and merge with multiple local and regional dust storms, often lasting tens of days.

Local dust storms can occur on Mars in any season at any location, although certain regional patterns have been identified [29–32]. Regional dust storms are particularly common during southern spring and summer seasons, occurring within a solar longitude range (L_S) between 180° and 360° (L_S = 0°, 90°, 180°, and 270° are defined as northern hemisphere spring equinox, summer solstice, autumn equinox, and winter solstice, respectively.), except during the solstitial pause period. These storms often concentrated in specific regions, such as Acidalia, Utopia, Arcadia, and Hellas [29]. Global dust storms, on the other hand, are unpredictable and non-periodic events in terms of both timing and location. Only seven confirmed global dust storms were observed in the years 1956, 1971, 1973, 1977, 2001, 2007, and 2018 [33].

In terms of seasonal and timescale characteristics, Martian regional-scale dust storms can be classified into three types: A, B and C [34], as illustrated in MY 36 shown in Figure 2a. The data presented in Figure 2 are derived from the global maps of the 9.3 µm absorption column dust optical depth (CDOD) database compiled by Montabone et al. [35,36] (refer to Section 3.3 for more details). It is important to note that types A, B, or C do not refer to specific dust storms but rather phases during the entire storm season, each potentially resulting from multiple regional and/or global dust storms. These storms are most active during the southern spring and summer seasons (L_S range 180°~360°), while the southern autumn and winter seasons (L_S range 0°~180°) generally experience lower dust activity levels.

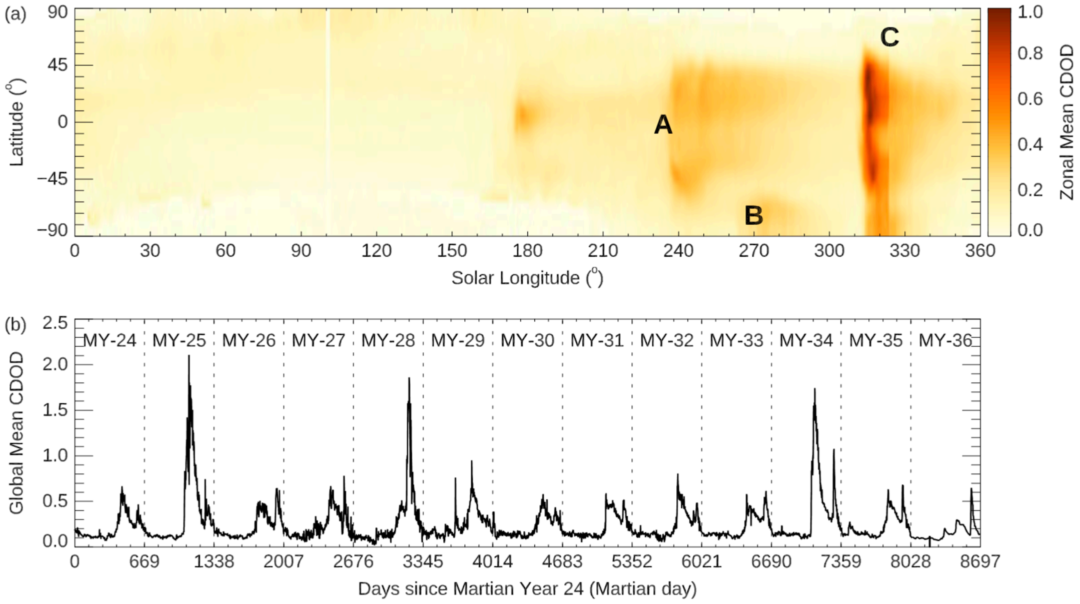

Figure 2. Variation of absorption column dust optical depth (CDOD) on Mars from MY 24 to 36. (**a**) An example of a zonal mean is 9.3 µm CDOD in MY 36. The three types of dust storms are denoted by A, B, and C. (**b**) Temporal variations of the global mean CDOD from MY 24 to 26.

Type A dust storms typically intensify in the middle and low latitudes between L_S = 180° and L_S = 270°, covering more than two-thirds of Mars' latitude and lasting approximately four months. Type A dust storms are characterized by their longer duration and broader coverage, with occasional evolution into global dust storms in certain Martian years (e.g., 2001, 2007, 2018). Near the end of a Type A dust storm, close to the summer solstice in the southern hemisphere, Type B dust storms erupt primarily in the south-polar region of Mars, lasting about two months. These storms are predominately local and regional, confined mainly to latitudes near the South Pole (south of 60° S). Following the conclusion of Type A and B dust storms, Type C dust storms typically occur around L_S = 330° in the middle and low latitudes, lasting one to two months. Type C dust storms may also develop into global dust storms that cease before the southern autumn equinox, marking a return to a calmer period and beginning a new cycle in the next Martian year.

Overall, Martian dust activity follows a seasonal pattern as described above. For example, Fourier analysis of long-term global mean CDOD during MY 24–36 (Figure 2b) reveals a precise periodicity of 668.615 days. However, there are significant irregular interannual variations in the intensity, frequency, onset, and duration of dust storms, as well as their impact range. This variability presents substantial challenges in predicting Martian dust storms. Furthermore, accurately quantifying the contribution of dust storms to atmospheric suspended dust levels indicated by CDOD remains challenging due to factors other than dust storms (e.g., dust devils, convections, gusts) contributing to atmospheric dust levels.

The effective radius of lofted dust particles on Mars is typically around 1.5 μm, but it varies depending on the intensity of dust storms. Weak local dust storms near the Martian northern summer solstice have particles averaging about ~1 μm in size, whereas, during regional and global dust storms in the southern spring and summer, particle size can increase to approximately ~2 μm, as observed by the Curiosity rover [37,38]. Generally, the effective radius of dust particles correlates with atmospheric dust content, with larger particles prevalent during the southern hemisphere's spring and summer compared to autumn and winter [39–41].

In the vertical direction (10–70 km height range), the distribution of dust particle sizes in the Martian atmosphere exhibits a bimodal pattern: the primary peak ranges from 0.7 to 1.2 μm, and a secondary peak ranges from 0.04 to 0.07 μm [42], as observed by the Spectroscopy for the Investigation of the Characteristics of the Atmosphere of Mars (SPICAM) instrument on Mars Express [43]. The altitude-dependent distribution of particle sizes significantly influences how incoming solar radiation is absorbed, scattered, and re-radiated, thereby impacting the radiative balance. These effects play a crucial role in large-scale atmospheric circulation and climate variability on Mars [44,45]. During the dust season, particularly following the onset of Type A dust storms, smaller dust particles tend to dominate the lower atmosphere and persist longer [25]. A higher proportion of smaller particles can intensify heating rates, temperatures, westerly winds, and meridional winds associated with the Hadley circulation [46]. Changes in meridional circulation due to adiabatic heating further contribute to temperature fluctuations on Mars [45].

2.2. Driving Mechanisms of Dust Storms

The interannual variability of dust storms during the southern hemisphere summer season significantly influences the seasonal climate on Mars. Therefore, it is crucial to understand the driving mechanisms behind these dust storms in order to comprehend Martian climate dynamics. In this section, we review the current understanding of the mechanisms responsible for dust lifting and the factors contributing to seasonal and interannual variability in dust storms.

The fundamental prerequisite for a dust storm is dust lifting. When Mariner 9 arrived at Mars in 1971, it observed the decaying phase of a global encircling dust storm from Martian orbit [47]. Subsequent studies have focused on elucidating the driving mechanisms of these storms. Leovy et al. [48] reviewed early work and proposed an energy balance model. During the southern hemisphere spring, local dust storms are initially generated by phenomena such as dust devils and cyclonic dust storms [49], intense surface winds in baroclinic regions [50], or strong mass outflow wind [51], which accumulate dust in southern, middle, and subtropical latitudes. Intense insolation, low static stability, and high atmospheric absorptivity and emissivity facilitate strong meridional circulations that can trigger global storm events [48]. Observations at the Viking Lander #1 suggested that local dust storms can also be triggered by baroclinic wave activity with a threshold wind speed of 25–30 m s^{-1} [52].

Dust particles are lifted through exchanges of momentum and heat between the Martian surface and atmosphere. Gierasch and Goody [49] initially proposed the existence of an axisymmetric swirling flow field around a central dusty core, where solar radiation heating strengthens horizontal temperature gradients, accelerating the cyclonic swirling flow inward into the core. Ryan and Lucich [53] further found that dust devils occur more frequently during the southern hemisphere spring and summer. The coexistence of multiple dust devils has been suggested as a possible mechanism for generating local dust storms [24,54]. Currently, two primary mechanisms are recognized for lifting dust particles: surface wind stress lifting and convective vortex lifting (such as dust devils), supported by various numerical simulations [55–59] using Martian global circulation models (GCMs) [60]. Dust particles are lifted during the saltation of more easily mobilized sand-size particles above a certain threshold [55,56]. It has been proposed that background dust haze on Mars is sustained by dust devil lifting [57,58]. Simulation studies combining convective schemes with high-threshold and high-rate stress lifting have successfully simulated spontaneous and interannually variable global dust storms [57]. Further simulations indicated that both wind stress and dust devil are essential and contribute equally to the total dust lifted [58].

Current consensus indicates that seasonal dust storms on Mars are primarily driven by variations in solar radiation forcing on the Martian surface and atmosphere system. In this system, the planetary boundary layer is recognized as playing a critical role in the Martian dust cycle [61]. As solar radiation increases near the southern spring equinox, it heats the lower Martian atmosphere, leading to accelerated atmospheric circulation. This enhanced near-surface wind stress lifts dust particles into the atmosphere [55,56], which in turn further heats the atmosphere and creates zonal temperature gradients. These gradients strengthen equatorial easterly winds, establishing positive feedback mechanisms that lift more dust particles into the atmosphere and ultimately result in large regional or global dust storms.

The mechanisms discussed above primarily pertain to the coupling of Mars' atmosphere and surface modulated by solar radiation. However, other potential mechanisms link dust storms to changes in Martian orbital and rotational motions, influencing atmospheric dynamics [12,62–65]. Shirley [12] found that all regional dust storms escalated into global dust storms during periods when Mars's orbital angular momentum relative to the solar system barycenter was increasing or at its maximum. Recent simulations [64,65] further illustrated that global dust storms occur around times of peak orbital-spin coupling torques and during periods of rapid torque changes. Orbital-spin coupling induces intensified, and relaxed circulations overlaid on the normal annual cycles of atmospheric circulation driven by external solar forcing. The asynchrony of these two cycles introduces interannual variability in dust storms [12,62–64].

To summarize, the precise mechanisms governing interannual variations in Martian dust storms, particularly global dust storms, remain unclear. Modeling efforts over recent decades have incorporated Mars global circulation models, such as the Mars GCM, e.g. [55,56] and the Ames Mars Global Climate Model (AMGCM), e.g. [58,66], achieving significant success by embedding dust lifting schemes. Detailed reviews on the status of the Martian whole atmosphere model and dust activities can be found in Wu et al. [67] and Zhou et al. [68]. Incorporating accelerations from orbit-spin coupling [65] into these models could further enhance their ability to replicate interannual variability in Martian dust storms.

2.3. Impacts of Dust Storms

Dust storms on Mars have profound effects on various aspects of the planet's environment and pose potential hazards for exploration and manned missions. Here, we review their impacts on atmospheric dynamics, atmospheric electrical properties, the space environment, topography, and Mars exploration.

During a dust storm, dust lifted into the atmosphere significantly absorbs solar radiation, causing temperatures in the Martian atmosphere to rise by at least 20 °C above the altitude of 25 km [69,70] while the surface temperatures decrease. The nighttime surface temperature is raised during the main phase of dust storms, making the diurnal temperature difference significantly lower during dust storms [71]. The radiation effect of dust changes the thermal structure and dynamic conditions of the atmosphere, which further affect the atmospheric tides and intensify meridional wind and Hadley circulation of Mars [72,73], strengthening the interhemispheric transport of dust. Furthermore, dust storms affect the sublimation and condensation of the CO_2 ice sheet in the polar region [74], thereby altering the atmospheric pressure.

Simulations, experiments, and calculations have demonstrated that Martian dust storms can generate friction discharge due to dust driven by strong winds, leading to low-frequency electromagnetic disturbances [75–78]. Additionally, during periods of high dust activities, the increased dust aerosols are favorable to attaching ions, resulting in a decrease in atmosphere conductivity [79,80].

The dust activities in the lower atmosphere will significantly influence the upper atmosphere, ionosphere and magnetosphere through vertical transportation and coupling. During dust storms, the rise in lower atmospheric temperature induces an increase in CO_2 density in the upper atmosphere [81,82]. As a result, the ionospheric peak height will be raised by tens of kilometers but without significant variation in peak electron density [83–85]. The variations of atmospheric ion densities are species-dependent, with CO_2^+ ions significantly increased, O^+ ions decreased, while no obvious change in O_2^+ ions [84]. More water vapor is transported to higher altitudes during dust storms. These water molecules undergo dissociation and ionization, which can lead to an increased hydrogen escape rate of 5–10 times [3,5,86]. At the same time, the escape rate is CO_2^+ ions can be increased by 3 times [83]. Apart from the strong orbital forcing on the vertical profile of water vapor saturation [87], dust storms will significantly increase vertical water vapor transportation, further depleting the ozone [88].

On the surface of Mars, dust storms have a direct impact on the topography. Dust storms can affect the deposition of dust [89] and volatile (ice/snow) [90] in the polar ice caps, which in turn can significantly influence the analysis of Mars' climate evolution history. Furthermore, dust storms are capable of driving the redistribution of dust across the Mars surface, and the strong winds (reaching speed of up to 100 km h^{-1}) play an important role in reshaping and evolving the topography and landform [91]. Additionally, dust storms also contribute to exposing organic matter in the surface soil that has not been degraded by cosmic rays, thereby aiding in assessing potential signs of life on Mars surface [92].

Apart from the environmental effects mentioned above, dust storms have a direct impact on the operations of landers and rovers on the surface of Mars [19]. The accuracy of landing will be reduced due to the large uncertainties in the atmospheric density, strong winds, and poor observing conditions during dust storms [93]. Martian dust particles range in size from 0.1 to 2000 μm and can take on plate-like, angle-like, or round shapes with a particle density of 2.6 to 3.0 g cm^{-3} [94]. They are rich in elements such as Si, Al, Fe, Mg, Ca, Ti, S, Cl, and Br [95]. These tiny dust particles can cover or penetrate the surface of instruments, causing mechanical failure and affecting the operation of related hardware and electronics. For example, dust activities have been shown to reduce the efficiency of solar panels and even cause damage [96–98]. When the atmosphere becomes dusty, the communication between Mars landers/rovers and Earth will be attenuated or even interrupted [99]. The Opportunity rover worked for fourteen years on Mars until it lost contact during the global dust storm in 2018. In December 2022, the National Aeronautics and Space Administration (NASA) announced that the Insight mission launched in May 2018 was ending due to power loss after a strong dust storm. Any landers or rovers using solar panels as their power source will be significantly impacted by dust storms and may even suffer fatal damages. Additionally, it has been found that Martian soil is rich in Cr (hexavalent chromium ions are highly toxic), S, and Cl elements [95,100]; therefore, Martian dust could be toxic and acidic, posing a significant threat to the health of astronauts. The great temperature, pressure, and wind variations during dust storms will significantly affect the entry, descending, and landing process and the returning process.

In summary, comprehensive monitoring and forecasting are essential for the study of Mars' multi-layer coupling system and for safe Mars exploration missions due to the significant impacts of dust storms on Martian environments and exploration activities.

3. Detection Methods for Dust Storms

In the 1950s, the global encircling dust storm on Mars was first observed through ground optical telescopes [101]. Since then, detection and investigation of dust storms have always been a primary focus of Mars exploration missions. This section reviews the detection methods for dust storms, with an emphasis on those performed by Martian orbiters and landers/rovers.

3.1. Historical Views on Dust Storms

Before human detectors arrived at Mars, qualitative observation and analysis of dust storms on Mars were mainly carried out using ground-based telescopes. The interannual variation characteristics of Martian dust storms have been identified; specifically, changes in color and albedo near the perihelion of Mars indicate frequent occurrence of large dust storms [22,23].

One of the crucial physical parameters for quantifying the content and spatial distribution of dust particles in the Martian atmosphere is the vertical profile of the dust optical depth (DOD). This parameter is associated with the attenuation of light in the propagation direction due to absorption and scattering (i.e., extinction) by dust particles in the atmosphere when the radiation of a specific wavelength passes through. The column-integrated DOD from the surface to the top of the atmosphere gives the CDOD, where a larger value indicates more serious attenuation and stronger dust activity. The vertical profile of optical depth can be retrieved from the radiation measured by a limb observation instrument, which offers important information about the vertical transport of dust. It should be noted that while relative changes in optical depth can be easily obtained from remote sensing observations, obtaining absolute values is much more challenging as it requires an accurate understanding of key properties related to dust, such as particle size distribution and optical parameters. In order to obtain CDOD for Mars, most US and European probes since Mariner 9 have been equipped with optical instruments capable of detecting dust storm activity, including spectrometers, radiometers, imagers/cameras, LiDAR, etc. Table 1 summarizes the dust-related measurements in Mars exploration history. Currently, methods for monitoring Martian dust storms can roughly be divided into three categories: orbiter multicolor cameras, orbiter infrared (IR) and/or ultraviolet (UV) spectrometers, and lander/rover cameras.

Table 1. Successful dust-related measurements in the Mars exploration history.

Mission	Type	Instruments	Years	References
Mariner 6	Flyby	IR Spectrometer (IRS)	1969	[102,103]
Mariner 7	Flyby	IR Spectrometer (IRS)	1969	[103]
Mariner 9	Orbiter	IR Spectrometer (IRS) UV Spectrometer (UVS) Television (TV)	1971~1972	[47,104,105]
Viking 1	Orbiter Lander	IR Thermal Mapper (IRTM) Visual Imaging Subsystem (VIS) Cameras	1976~1980 1976~1982	[106,107]
Viking 2	Orbiter Lander	IR Thermal Mapper (IRTM) Visual Imaging Subsystem (VIS) Cameras	1976~1978 1976~1980	[106,107]

Table 1. *Cont.*

Mission	Type	Instruments	Years	References
Mars Global Surveyor (MGS)	Orbiter	Thermal Emission Spectrometer (TES) Mars Orbit Camera (MOC)	1997~2006	[108–110]
Mars Pathfinder	Lander Rover	Imager for Mars Pathfinder (IMP) Atmospheric Structure Instrument Navigation Camera (ASINC) Alpha Proton X-Ray Spectrometer (APXS)	1997 1997	[95,111,112]
Mars Odyssey	Orbiter	Thermal Emission Imaging System (THEMIS)	2004~present	[113]
Mars Express	Orbiter	Spectroscopy for the Investigation of the Characteristics of the Atmosphere of Mars (SPICAM) Observatoire pour la Mineralogie, l'Eau, les Glaces et l'Activité (OMEGA) High Resolution Stereo Camera (HRSC)	2003~present	[43,114–116]
Mars Exploration Rovers: Spirit Opportunity	Rover Rover	Panoramic Cameras (Pancam) Miniature Thermal Emission Spectrometer (Mini-TES) Alpha Particle X-ray Spectrometer (APXS)	2004~2009 2004~2022	[117–119]
Mars Reconnaissance Orbiter (MRO)	Orbiter	Mars Color Imager (MARCI) Compact Reconnaissance Imaging Spectrometer for Mars (CRISM) Mars Climate Sounder (MCS)	2006~present	[120–122]
Phoenix	Lander	Surface Stereo Imager (SSI)	2008~2009	[123]
Mars Science Laboratory (MSL) Curiosity	Rover	Rover Environmental Monitoring Station (REMS) Mast Camera (Mastcam)	2012~present	[41,124]
ExoMars 2016 Trace Gas Orbiter (TGO)	Orbiter	Nadir and Occultation for Mars Discovery (NOMAD) Color and Stereo Surface Imaging System (CaSSIS) Atmospheric Chemistry Suit (ACS)	2016~present	[125–127]
Insight	Lander	Color Cameras Auxiliary Payload Sensor Suite	2018~2022	[128,129]
Perseverance	Rover	Mastcam-Z SuperCam Mars Environmental Dynamics Analyzer (MEDA)	2021~	[130–132]
Hope	Orbiter	Emirates Exploration Imager (EXI)	2021~	[133]
Tianwen-1	Orbiter	High-Resolution Imaging Camera (HiRiC) Medium Resolution Imaging Camera (MoRiC) Multispectral Camera (MSCam)	2021~	[134–136]

3.2. Orbiter Multicolor Imaging

Optical imaging is a valuable tool for monitoring the occurrence and development trends of dust storms on Mars. It provides the most intuitive way to track dust storm activities. Two important cameras, the MGS MOC [108,109] and the MRO MARCI [120], have been operated on Mars orbiters. These instruments have provided daily global maps of Mars from 1999 to the present, offering an extensive database for investigating Martian dust storms [28,29,137]. More recently, the EXI instrument on the Emirates Mars Mission (EMM) Hope mission [133] has been acquiring both regional and global images in a completely different orbit with different spatiotemporal coverage compared to MGS and MRO [138].

The most successful imager in Mars orbit is the MARCI onboard MRO. The MRO operates in a polar near-circular orbit of Mars, with an apogee of approximately 320 km and a perigee of around 255 km. At this altitude, large-field optical images with a spatial resolution of 1~10 km can be obtained. With the help of Mars' rotation, a global image of Mars can be captured every day. The wave bands covered by MARCI range from ultraviolet to visible and near-IR bands, which are selected by seven filters with central wavelengths of approximately 260 nm, 320 nm, 425 nm, 550 nm, 600 nm, 650 nm, and 725 nm, respectively [120]. MARCI operates in push-frame mode, with the camera's optical axis always pointing at the nadir point. The cross-track field of view (FOV) is 180° while the along-track FOV is 26° for the visible and near-IR channels and 20° for the ultraviolet channel, respectively [120]. The angular resolution is 0.13° in both along-track and cross-track directions [120].

The design of MARCI is very sophisticated, utilizing a dual optical path single-focal plane design. The optical system of the visible and near-IR channels and the ultraviolet channels are independent to ensure the transmittance of different channels and optical image quality. In front of the Charge Coupling Device (CCD), two prisms were utilized to redirect the beams at different wavelengths to the appropriate parts of the CCD based on the principle that light with different wavelengths has different refractive indices in the same medium. Furthermore, according to the focusing position of different bands on the CCD, narrowband interference multilayer filters are directly deposited on the CCD's photosensitive surface. This further realizes a narrowband filter and suppresses light crosstalk of different wavelengths while enabling simultaneous imaging of different wavelengths, which is essential for joint scientific research involving multi-band images. These ingenious designs significantly reduce the size and weight of MARCI. The volume is controlled within 10 $cm^{3,}$ and the weight is controlled under 1 kg [120]. These specifications align with the requirements of having a small volume and light weight in deep space exploration.

The images of each band can be individually utilized for the study of the Martian atmosphere and surface. This includes analysis of clouds, circulation, dust storms, atmospheric ozone, polar surface processes, local albedo properties, surface color properties, mineralogical constraints, and surface physical constraints. For example, the images at wavelengths around 425 nm, 600 nm and 725 nm have been synthesized to create global color images of Mars (Figure 1b,c) in order to identify the ranges and evolution paths of dust storms [29], which are of great significance for revealing the generation and evolution laws of dust storms on Mars, especially the regional characteristics and spatiotemporal evolution laws of large dust storms. Based on the Mars Daily Global Maps (MDGM) from MGS MOC and MRO MARCI [139], a comprehensive Mars Dust Activity Database (MDAD) covering eight MYs (24~32) has been compiled. This database includes records of 14,974 dust storms with an area greater than 10^5 km^2 [140]. Analysis using this database by Battalio and Wang [140] revealed that many dust storm sequences originated from the northern mid-latitudes before flushing into the southern hemisphere across the equator following more coherent tracks (Figure 3). In contrast, sequence paths were found to be less organized in the southern hemisphere.

Recently, the Tianwen-1 orbiter from China was equipped with a MoRiC [135], which is a standard RGB color camera. The main objective was to capture images of the surface of Mars, produce global remote sensing images of Mars, explore the topography and changes of Mars, and study the geological structure, topography, and landforms. MoRIC had a FOV of 53.3° × 41.2° and provided a spatial resolution at a nadir point of about 98 m at an orbital altitude of 400 km [135]. Dust storms were directly observed in the images captured by MoRIC (as shown in Figure 1a). The Tianwen-1 orbiter was also equipped with a HiRiC capable of acquiring images with a spatial resolution of ~1 m [134]. The HiRiC was primarily used to obtain detailed images of key areas on the Martian surface, especially to determine the Tianwen-1 landing site [141].

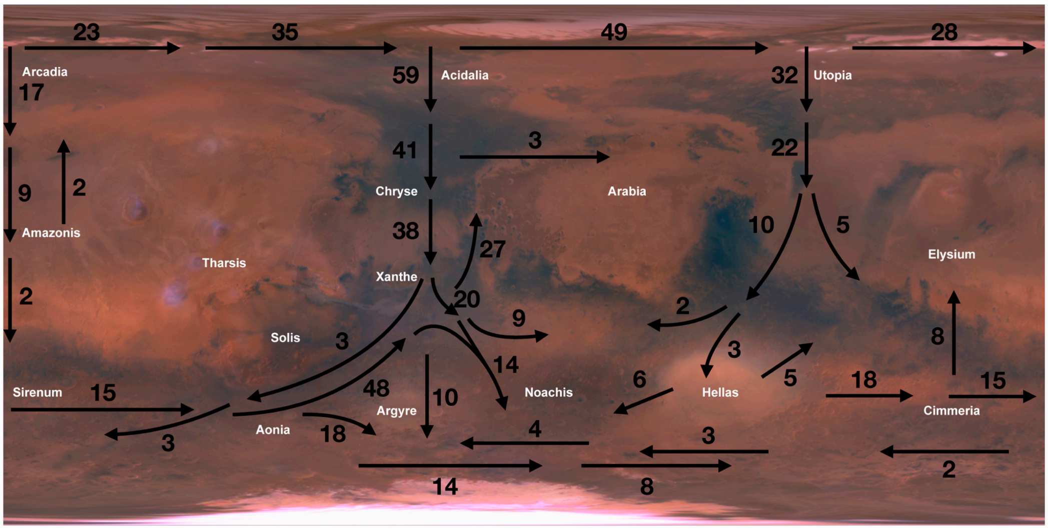

Figure 3. Paths of dust storm sequences observed by MGS MOC and MRO MARCI during MY 24 and 32. The numbers near the arrows indicate the number of sequences traveling along that path. (Adapted from Battalio and Wang [140]).

3.3. Orbiter Infrared Spectroscopy

The visible light images captured by the orbiter cameras can monitor the global distribution and spatiotemporal changes of the dust storms (e.g., area, lifetime, and moving speed), but there are challenges in quantitatively estimating the strengths of dust storms without an accurate Martian surface albedo model. Herein referred to as the strength of a dust storm, it is mainly related to the amount of dust in the atmosphere, namely dust opacity profile and CDOD. With this parameter, particularly through global measurements, the area, lifetime, and moving speed of dust storms can be estimated. A time series analysis using this parameter is also crucial for atmospheric numerical simulations. Currently, IR spectrometers and radiometers are primarily used to estimate dust optical depth from Mars orbit due to their greater sensitivity at larger optical depths.

The observation of IR spectra by Mars orbiters has a long history, dating back to Mariner 6 & 7 [102,103]. With the maturation of IR spectroscopy and radiative transfer models, starting with the MGS, NASA's Mars orbiters have been equipped with IR/thermal IR spectrometers to continuously monitor the Martian atmosphere and dust storms. These instruments include the TES on MGS [110], the THEMIS on Odyssey [113], and the MCS on MRO [122]. Together, these three spectrometers have provided continuous and complete quantitative monitoring data of global dust activities on Mars since MY 24 (1998–present). Apart from THEMIS, which just adopted the nadir viewing mode, both TES and MCS adopted scanning mode to realize nadir and limb observations [142]. The SPICAM on Mars Express [43] was an ultraviolet-IR (UV-IR) dual spectrometer, which was the first instrument to perform stellar occultations at Mars in order to retrieve aerosol vertical distributions [114]. Recently, data from the OMEGA instrument [115] on Mars Express were also used to retrieve DOD [143].

The basic method for retrieving DOD in infrared involves searching for optimized profiles of temperature, dust, and water ice that best match observed radiation profiles based on the radiative transfer models of the Martian atmosphere. Nadir viewing data can be used to retrieve the CDOD, while the limb viewing data can be used to retrieve vertical profiles of DOD. Both retrieving processes must consider the contributions of temperature and other aerosols such as water, ice, and CO_2. To retrieve CDOD from the nadir view, the general radiative transfer equation is [144–146]

$$I_{obs}(\nu) = \epsilon(\nu) B\left[\nu, T_{surf}\right] e^{-\frac{\tau_0(\nu)}{\mu}} + \int_0^{\tau_0(\nu)} B[\nu, T(\tau)] e^{-\frac{\tau(\nu)}{\mu}} d\tau, \tag{1}$$

where $I_{obs}(\nu)$ represents the observed monochromatic radiance of Mars at wave number ν, $\epsilon(\nu)$ is the surface emissivity at wave number ν, $B[\nu, T(\tau)]$ stands for the Planck function, $\tau_0(\nu)$ denotes the normal column-integrated aerosol optical depth, μ is the cosine of emission angle, T_{surf} is the surface temperature, $T(\tau)$ refers to the atmospheric temperature. The integration is performed from the spacecraft to the surface. The total aerosol optical depth is mainly contributed by dust particles, water ice, and CO_2. Assuming a plane-parallel atmosphere and uniform mixing of dust, water, ice, and CO_2, Equation (1) can be solved to obtain CDOD.

To retrieve the vertical profiles of temperature, dust, and water ice, Kleinböhl et al. utilized a modified Chahine method and a fast radiative transfer scheme based on the Curtis-Godson approximation [147]. The basic radiative transfer equation is

$$R = \int_{\nu} F(\nu) \int_{z} B(\nu, T(z))K(\nu, z)dzd\nu \tag{2}$$

where R is the radiance seen at a specific viewing direction in a certain channel, $F(\nu)$ is the frequency response function of the channel, and $K(\nu, z)$ is the vertical response function at frequency ν, respectively. This retrieving algorithm was successfully applied to the MCS onboard the MRO.

Apparently, the CDOD obtained from observed radiance at different wavebands will have different values. For example, the 9.3 µm CDOD represents dust-induced absorption at 9.3 µm, while the 21.6 µm CDOD represents dust-induced absorption at 21.6 µm [147]. The 21.6 µm CDOD can be converted to 9.3 µm CDOD by multiplying a factor of 2.7 [35]. The CDOD retrieved from TES, THEMIS, MCS, and other IR spectrometers listed in Table 1 formed the most important and the longest time series of daily global maps of CDOD, which significantly improved our understanding of the climatology of Martian dust storms [36]. These daily global column-integrated dust scenarios greatly benefited the numerical simulations of the Martian climate system, e.g. [36,148]. Strong diurnal variations in the vertical distribution of dust during the global dust storm in 2018 were observed by MRO MCS and were attributed to meridional circulation exhibiting diurnal tidal variations [149]. Fast changes in water abundance observed by TGO NOMAD during the same storm suggested that the impact of dust storms on the Martian atmosphere is very fast [150]. Based on retrieved dust, temperature, ice, and water profiles during the Type C dust storm in January 2019, it was found that regional dust storms can enhance Martian water loss to space by a factor of five to ten [3]. It should be pointed out that, in this work [3], water vapor was measured by TGO ACS and NOMAD higher up, while MCS estimated water vapor in the middle atmosphere by assuming that vapor was at its condensation threshold given by their measured temperature.

3.4. Landers/Rovers Monitoring

On the surface of Mars, the visible solar radiations received can be utilized to measure dust storm activity. According to the Beer-Lambert Law, the solar radiation flux (F) reaching the Mars surface can be expressed as $F = F_{\mathrm{TOA}} \times e^{-\tau\eta}$, where τ represents the visible CDOD (VDOD), F_{TOA} is the solar radiation flux at the top of the atmosphere, and η denotes the airmass [117]. This method has been successfully applied on MER Opportunity and Spirit rovers, as well as other landers/rovers. The panoramic cameras on both rovers routinely image the Sun near local noon each day on Mars at 440 nm and 880 nm [117,118]. Other small multispectral cameras on the landers/rovers, such as SSI [123], Mastcam [124], and Mastcam-Z [130], are all valuable for dust storm monitoring, not only for DOD but also for surface property and mineral characteristics.

The VDOD retrieved from two wavelengths are nearly identical, as demonstrated by the VDOD series during the lifetime of the Opportunity rover in Figure 4. The Opportunity rover survived the global dust storm in 2007 but, unfortunately, was completely lost during the global dust storm in 2018. Images taken by Opportunity rover during the eruption of this 2018 global dust storm clearly show drastic attenuation of visible solar radiations on Mars' surface due to the strong absorption of dust particles (Figure 5). When VDOD reached 11, the visible light can be attenuated by nearly 100%, with IR band attenuation also at 98%, resulting in a darkened Martian surface.

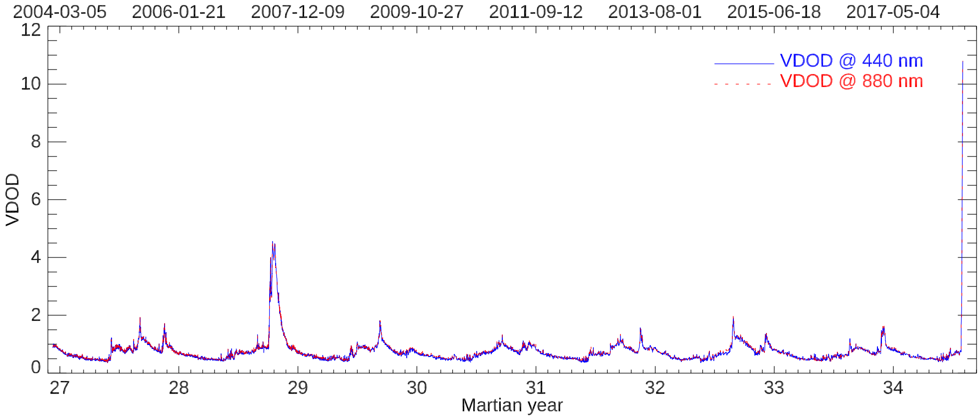

Figure 4. The VDOD was recorded by the Opportunity rover. VDOD observed in 440 nm (blue solid) and 880 nm (red dashed) are shown.

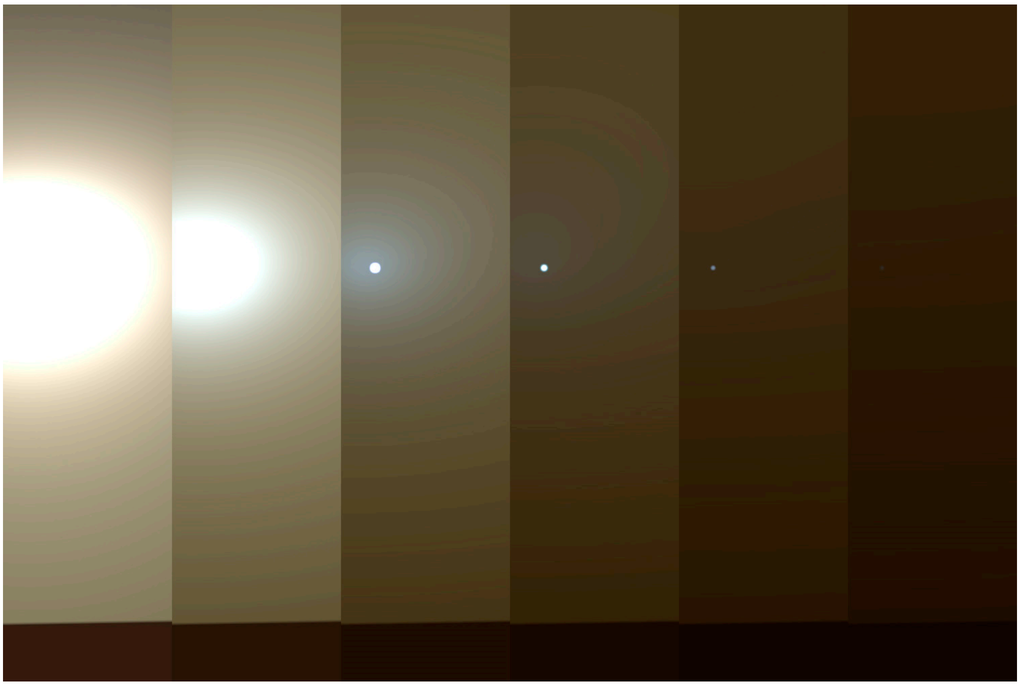

Figure 5. Photographs of the Sun in visible light captured by the panoramic camera onboard Opportunity rover during the eruption phase of the global dust storm in June 2018. The VDOD for each frame is 1, 3, 5, 7, 9, and 11, from left to right. (Image taken from https://www.jpl.nasa.gov/images/pia22521-shades-of-martian-darkness, accessed on 15 May 2024. Credit: NASA/JPL-Caltech/TAMU).

Based on the operation status and record of landers and rovers on Mars over the past two decades, it has been observed that different levels of dust storms have varying effects on the landers/rovers. The engineering team at NASA has developed a guidebook for dust storm operations [99], which classifies dust storms into six levels based on VDOD values, as outlined in Table 2.

Table 2. Classification of dust storm levels according to VDOD values [99].

Levels	VDOD Values	Actions
Level 1	<0.7	No restrictions.
Level 2	0.7 < VDOD < 1.0	No restrictions but watch the VDOD closely.
Level 3	1.0 < VDOD < 2.0	Scientific activities can only be carried out within reasonable limits during the day, with no overnight activities, and the operation team searches for possible parking points for rovers and protective measures for landers.
Level 4	2.0 < VDOD < 3.0	Start driving to a parking point to safely ride out the dust storm, allowing ONLY essential activities (VDOD observation and battery control board history).
Level 5	3.0 < VDOD < 3.5	Final drive to parking point, minimal activities ONLY (VDOD observation and battery control board history), begin ultra-high frequency (UHF) overflights per a couple of days, and wait for VDOD to drop.
Level 6	VDOD > 3.5	Minimal activities ONLY (VDOD observation and battery control board history), UHF overflights per couple of days, and wait for VDOD to drop.

It is important to note that the trend of large dust storms is different to predict, making continuous monitoring and treatment according to the actual situation particularly crucial. For example, during the 2017 global dust storm, it took four days for the VDOD value to increase from 1 to 2, while it only took one day during the 2018 global dust storm. The rapid growth of the dust storm made following a guidebook impossible.

For landers/rovers using solar arrays as their power source, dust storms—especially global dust storms—can dramatically accelerate the rate of dust deposition, leading to a rapid degradation of power supply. The average decrease rate in the power supply due to dust accumulation is 0.2% per Martian day [96]. During large dust storms, however, the dust can be seasonally removed benefit from the large winds. The loss of solar energy mainly results from decreased solar insolation. During the 2018 global dust storm, when the VDOD values increased from 0.6 to 10.8 in eight days (3–10 June 2018), energy output from solar arrays dropped by an alarming 96.7% [99]. From 10 June, the Opportunity rover was officially dead, successfully exploring Mars for 15 years. These missions have provided valuable lessons: seasonal dust storms have significant impacts on landers/rovers, and real-time monitoring of the dust storm activities—from both orbiters and landers/rovers—is crucial for ensuring security and successful scientific explorations on Mar’s surface.

4. Dust Storm Monitoring and Predicting for Tianwen-3

China has announced the implementation of a Mars sample return mission around 2030 [151]. Throughout the entire mission, the entry, descending and landing process, sampling process, and the launch process on the Martian surface are highly likely to be affected by Martian dust storms. In this section, we will discuss the potential characteristics of dust storm activity during the Tianwen-3 mission and propose a dust monitoring scheme for Tianwen-3.

4.1. Statistical Predictions

Based on long-term observation data of dust storms, primarily the CDOD retrieved from TES, THEMIS, and MCS, Montabone et al. [35,36] conducted systematic data processing, cross-calibration, and quality control on these data and established a comprehensive CDOD database covering MY 24 to present. The database is global, with a spatial resolution of 6° (longitude) by 5° (latitude) and a temporal resolution of one Martian day. The CDOD data in the database are all 9.3 μm CDOD. The 9.3 μm CDOD is converted to VDOD by multiplying a factor of 2.7 [35,152] to facilitate the assessment of the degree of dust storm impact according to the classification criteria in Table 2.

The sampling will take place in flat areas in the low-latitude regions in the northern hemisphere. Based on recommended landing site candidates, four zones in the northern hemisphere have been selected for statistical prediction of the dust storm levels using the following procedure:

- The four zones are located in Utopia Planitia, Isidis Basin, Amazonis Planitia, and Chryse Planitia, respectively. Each zone covers a range of 18° in longitude and 15° in latitude, creating a 3×3 grid in the VDOD database;
- The VDOD data in the grid during MY 24–35 (12 MYs) are extracted from the database to form a subset for each region, resulting in 108 samples for each zone ($=3 \times 3 \times 12$);
- For each Martian day, the numbers of the six dust activity levels in the 108 samples are counted, and their probabilities are calculated;
- Since Martian dust storms are seasonal, we extend the date to MY 40 and 41 according to the orbit of Mars;
- Finally, the predicted results are presented in Figure 6.

Taking the zone in Utopian Planitia as an example (Figure 6a), it is observed that:

- Before the southern spring equinox ($L_S < 180°$), the dust activity remains weak, generally below the safety line (VDOD < 1.0), occasionally exceeding 1.0 but with very short duration;
- After the southern spring equinox ($L_S > 180°$), there is a significant increase in the probability of VDOD exceeding 1.0. The trend is particularly noticeable between L_S of 200°~240° (i.e., 7 October to 11 December, 2029 in MY 40 and 25 August to 29 October, 2031 in MY 41), with the probability of VDOD exceeding 2.0 being greater than 30%. Dust activity generally peaks near L_S of 210°~220°, and then begins to weaken and recover. During this period, it is important for operators to closely monitor the changing trend of dust activity;
- After the southern summer solstice ($L_S > 270°$), dust activity experiences a significant weakening but remains at an active level. As shown in Figure 6a, just before $L_S = 270°$, the probabilities for Level 2 and Level 3 are both about 50%. Subsequently, dust activity will recover to quiet conditions and begin another seasonal trend.

In general, prior to July–September 2029 in MY 40 or May–July 2031 in MY 41, the overall level of Martian dust storms is very low, making it relatively safe to conduct sampling and returning activities during these periods. However, after July–September 2029 in MY 40 or May–July 2031 in MY 41, a significant increase in regional or global dust activity may significantly impact sampling and returning activities. A comparison between different zones in Figure 6 indicates that higher latitudes generally experience lower levels of dust activity compared to areas near the equator. It is therefore recommended that higher latitudes be selected as far as scientific requirements and engineering technology allow while completing the relevant science and engineering tasks by July 2029 or May 2031.

It is important to note that Figure 6 represents a preliminary statistical analysis, providing an initial reference for engineering task planning. It is recommended that other dust storm databases (such as the MDAD) be considered in conjunction with this analysis to ensure comprehensive and robust results. For instance, although Figure 6d indicates relatively low probabilities of Levels 2 and 3, it should be noted that Chryse Planitia lies in the middle of the paths of the outstanding dust storm sequences flushing into the southern hemisphere (Figure 3). Therefore, safety evaluations in this region should be conducted using multiple databases if the landing site is determined in the future. In order to minimize the impact of dust storms on the Mars sample return mission, it is essential to establish a Mars dust storm monitoring and early warning system prior to mission implementation [20]. Besides, once the landing site and window for Tianwen-3 are determined, dynamic forecasting methods, such as those proposed by Montabone and Forget [154], can be done in the future.

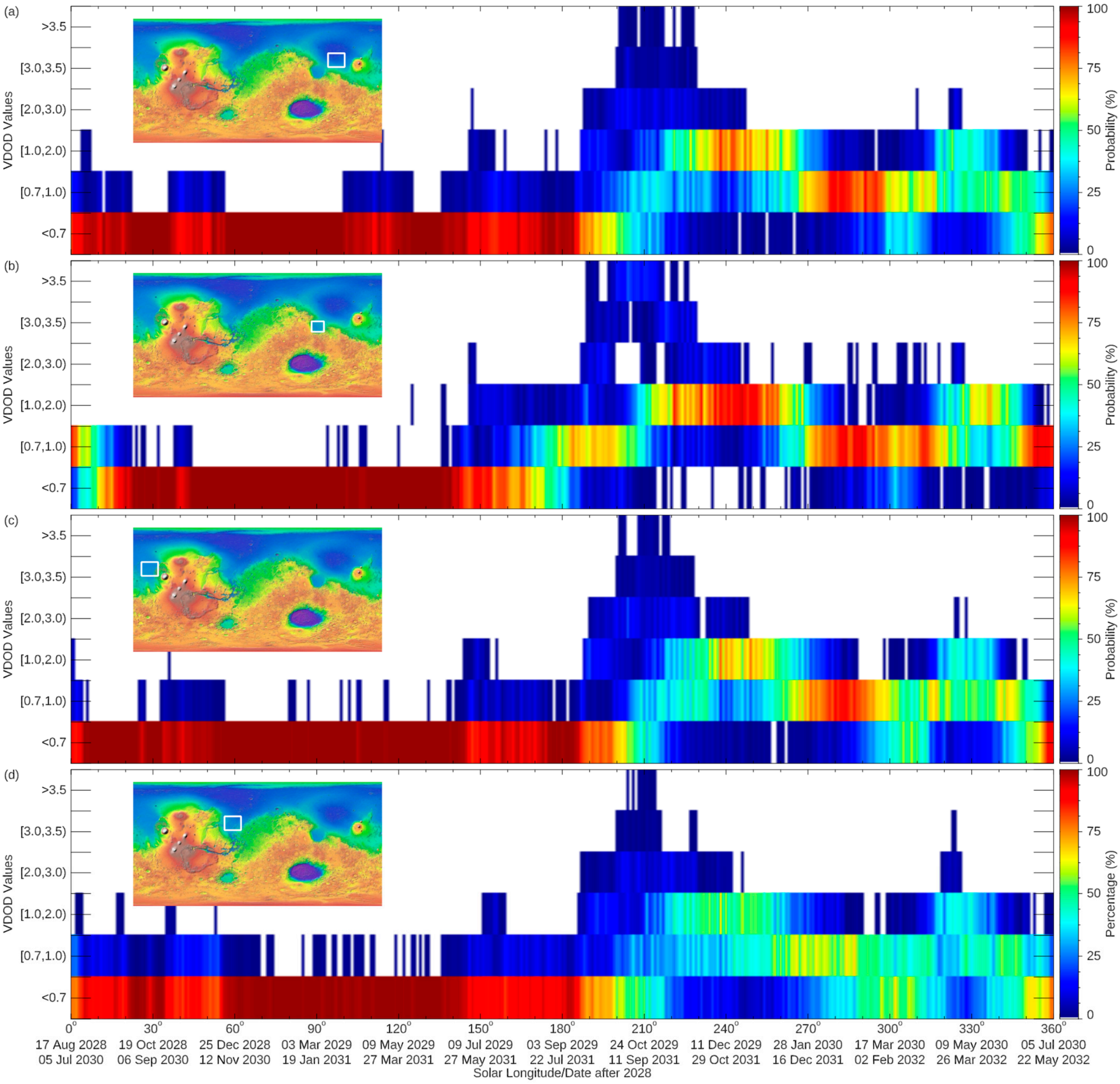

Figure 6. Statistical predictions of the dust storm activity level at five zones in the low-latitude regions of Mars. (**a**) Utopia Planitia, (**b**) Isidis Basin, (**c**) Amazonis Planitia, and (**d**) Chryse Planitia. Modified from He et al. [153]. The white rectangles represent the area of 3 × 3 grid used in the statistics.

Using the aforementioned method, we further statistically predicted dust storm activity levels across the entire northern hemisphere (Figure 7). The Martian year was divided into six periods, each spanning a L_S interval of 60° as shown at the top of each panel in Figure 7. Probabilities for each dust activity level during each period were then calculated within zones having a longitudinal range of 6° and a latitudinal range of 5°. The six rows in Figure 7 correspond to Level 1 to Level 6 from top to bottom.

Before the southern spring equinox ($L_S < 180°$), the dust activity is generally weak throughout the entire northern hemisphere, remaining below the safety line (VDOD < 1.0) as shown in Figure 7(a1–a3,b1–b3). Regions for VDOD > 1.0 are primarily concentrated in the Tharsis Montes, Chryse Planitia, and Utopia Planitia for $L_S < 60°$ (Figure 7(c1)), in the polar region for $60° < L_S < 180°$ (Figure 7(c2,c3)), and in low latitude regions for

$120^\circ < L_S < 180^\circ$ (Figure 7(c3)). However, these occurrences have a probability of less than 10%.

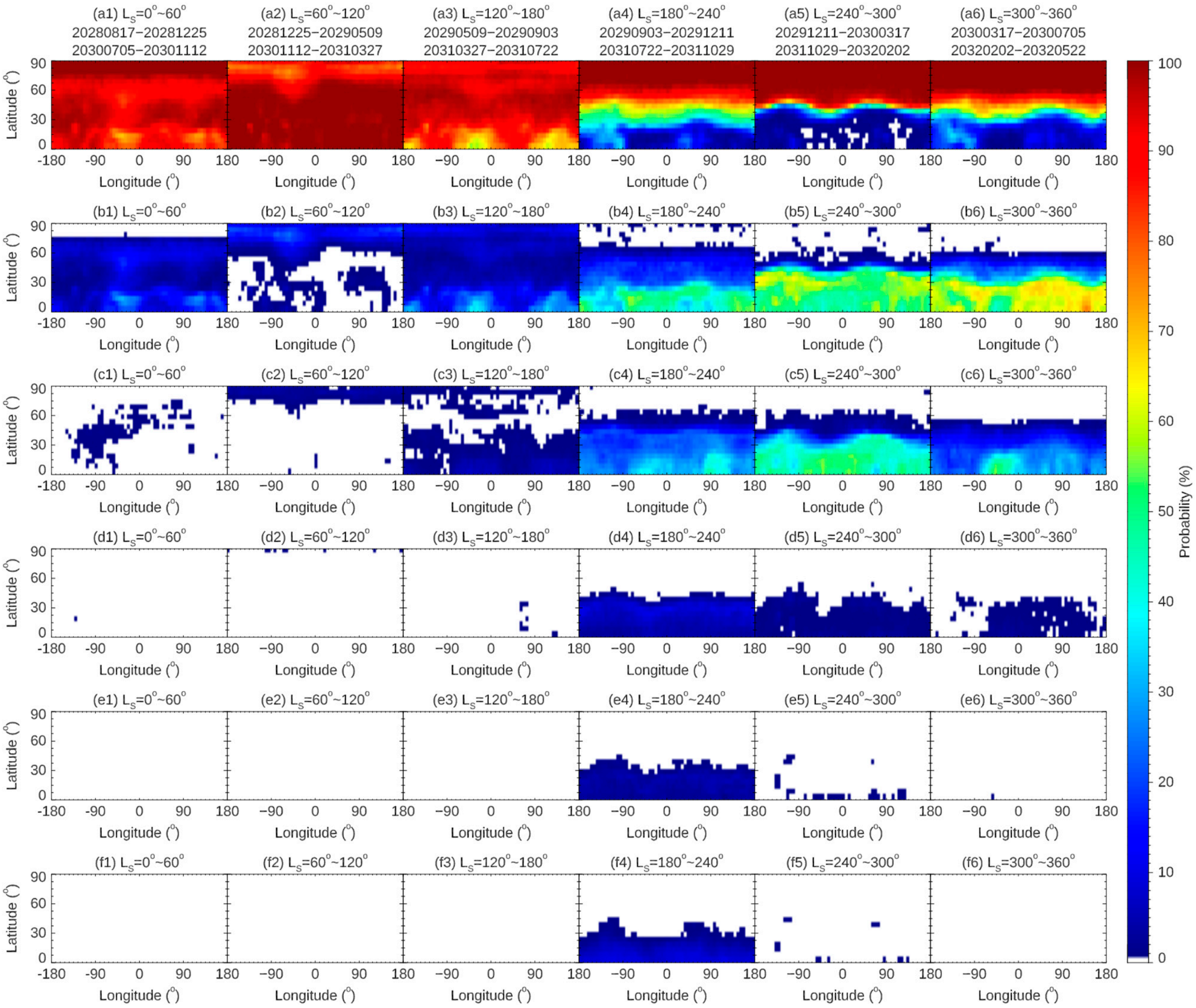

Figure 7. Statistical predictions of the VDOD levels (Table 2) in the entire northern hemisphere. (**a1**–**a6**) Probability for Level 1. (**b1**–**b6**) Probability for Level 2. (**c1**–**c6**) Probability for Level 3. (**d1**–**d6**) Probability for Level 4. (**e1**–**e6**) Probability for Level 5. (**f1**–**f6**) Probability for Level 6. The color bar is shown on the right. The L_S ranges are shown at the top of each panel. The date ranges in MY 40 and 41 are shown at the top of the first row. White areas indicate a zero probability.

Following the southern spring equinox ($L_S > 180^\circ$), the VDOD remains low in the high latitude regions but increases in the low latitudes, especially below the latitude of 30°. In the latitudinal belt of 0°~25°, the probabilities for Level 3 are 16%~46% ($180^\circ < L_S < 240^\circ$ in Figure 7(c4)), 29%~56% ($240^\circ < L_S < 300^\circ$ in Figure 7(c5)), 14%~55% ($300^\circ < L_S < 360^\circ$ in Figure 7(c6)), respectively, with the situation the most serious around the southern summer solstice (Figure 7(c5)). In Figure 7(c4), the peak is located in the Isidis Basin and the south of Utopia Planitia. In Figure 7(c6), the peak is located in the south of Chryse Planitia, which is in the middle of the paths of the outstanding dust storm sequences flushing into the southern hemisphere [140]. The probabilities for activities higher than Level 3 are generally below 10%. Extreme activities (higher than Level 4) are predominantly observed between $180^\circ < L_S < 240^\circ$, primarily attributed to the two global dust storms in MY 25 (2001) and MY 34 (2018). The global dust storm in MY 28 (2007, $270^\circ < L_S < 300^\circ$) was stronger in the southern hemisphere and thus not conspicuous in Figure 7(e5,f5).

4.2. Dust Storm Monitoring for Tianwen-3

During the sampling and returning phases of the mission, an orbiter will be utilized to provide high-resolution mapping of the landing site and measurements of environmental parameters, including dust storm activity. We have proposed to carry a Mars Multicolor Camera (MMC) to monitor dust storms because of the simplicity of instrumentation (e.g., lower power and mass and data rates). The main scientific objectives of MMC are as follows:

- Martian dust storm monitoring and early warning: Conducting large-field multicolor imaging of mid-low latitude dust storm activities on Mars to obtain information such as location, coverage and moving speed of dust storms on Mars.
- Spatial and temporal distribution of atmospheric ozone on Mars: Conducting large-field ultraviolet imaging of the column content of middle- and low-latitude ozone on Mars to obtain its spatial and temporal distributions. This will also improve the accuracy of dust storm identification in combination with water-ice cloud identification in visible light channels.

The Tianwen-3 orbiter is expected to operate in a circular orbit with an altitude of approximately 350 km, an orbital inclination of around 30°, and an orbital period close to 1.8 h. This orbit is an idea for global imaging of Martian dust storms at the middle and low latitudes. At this altitude, a camera with a FOV of 130° will achieve the largest surface coverage of ~3000 km cross-track. Considering the rotation of Mars, a global image of Mars will be generated each Martian day, covering an area below 52° latitude in both hemispheres, as indicated by the white circles in Figure 8. Due to the combined effects of orbital motion and Mars rotation, the revisit times for MMC over the same area are shown in Figure 9.

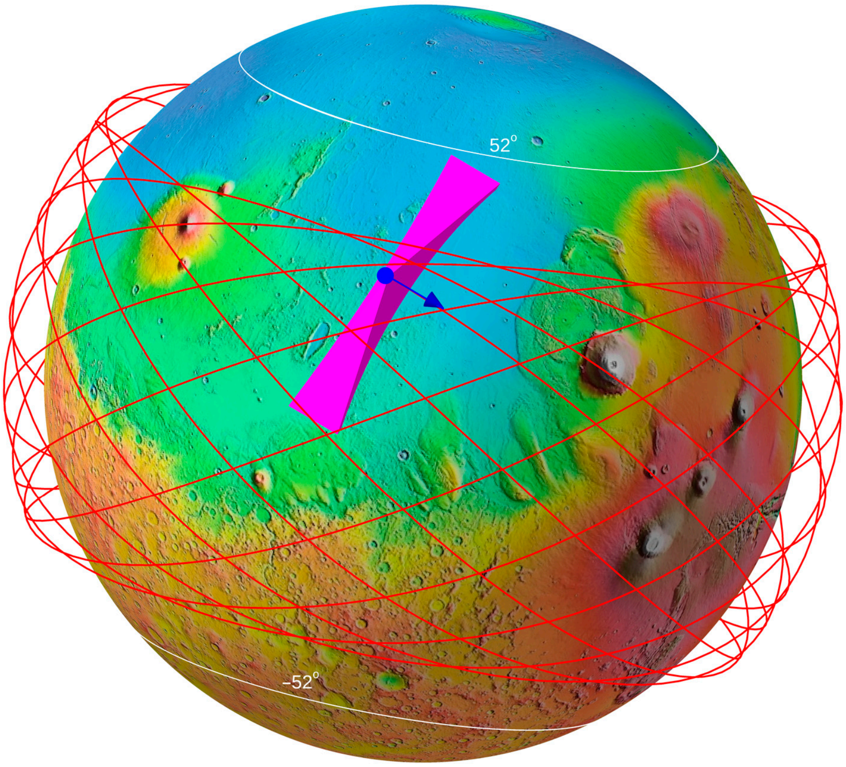

Figure 8. A demo of the orbit of the Tianwen-3 orbiter. The orbit is plotted by red lines. The orbiter is denoted by the blue dot, and its velocity is shown by the blue arrow. The pink surfaces demonstrate the FOV of the MCC. The background Mars digital elevation map is available at the U.S. Geological Survey Astrogeology Science Center (https://astrogeology.usgs.gov/search/map/Mars/, accessed on 17 May 2024).

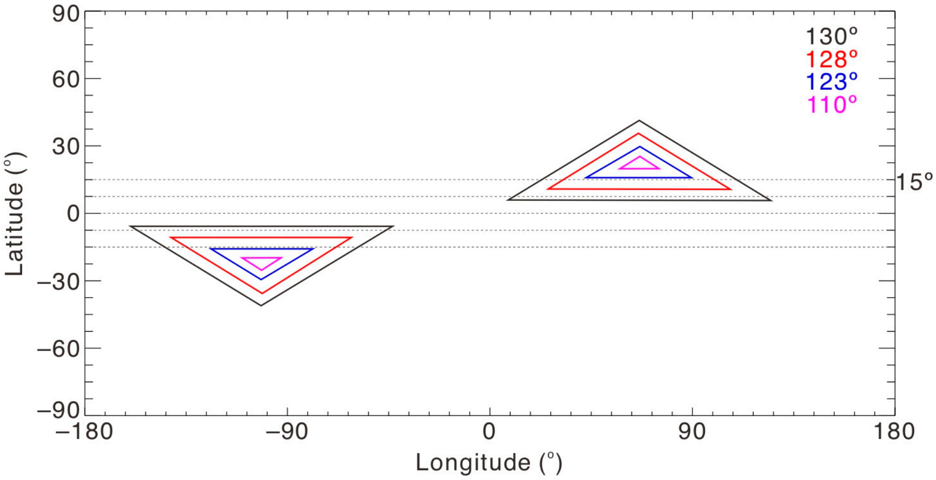

Figure 9. The surface areas can be revisited by MMC six times during Martian daytime with different cross-track FOV as shown by different colors.

The rotation period of Mars is ~24.62 h, and the orbital period of the Tianwen-3 orbiter is ~1.8 h. It is important to consider the coverage of the MMC FOV to the same area during the daytime period of each Martian day. As shown in Figure 9, an area of about 2000 km × 3000 km below 30° latitude can be continuously observed during six orbits throughout the daytime of each Martian day. In other words, for such an area of 2000 km × 3000 km, the MMC can achieve continuous monitoring with a time resolution of better than 2 h. Other regions with latitude lower than 30° in both hemispheres will be revisited at least three times during one Martian day. This is of great significance for early warning and prediction of dust storms during the landing, sampling and return phases of the mission.

The revisited area for different cross-track FOV of MMC is further shown in Figure 9. When the cross-track FOV decreases from 130° (black) to 110° (pink), there is a significant reduction in the area that can be revisited by MMC six times. When the cross-track FOV is smaller than 110°, no area can be revisited six times over. Therefore, it is determined that the cross-track FOV of MMC should achieve 130°. The along-track FOV is not so critical since the MMC will operate in a push frame mode, and it will be kept as small as feasible to reduce the data rate. Currently, the along-track FOV is determined to be 20°. We propose that once the landing and sampling site is determined, the tilt of the orbit should be as small as possible, and the orbital phase of the orbiter should be optimized to revisit the landing site six times or more.

For the demonstration orbit depicted in Figure 8, the westward longitudinal drift speed of the orbit in Mars body-fixed coordinate is ~24.8° per orbit. As a result, there will be a time difference of ~1.5 h between the orbital regression period and the Mars rotation period, and the opportunity for six observations per day will have a time interval of ~15 Martian days. If the orbital altitude is slightly decreased to ~300 km (although this may lead to a slight decrease in cross-track FOV coverage), and the orbital period is shortened to ~1.76 h, this time difference between the orbital regression period and the Mars rotation period will be reduced to only 0.02 h, making it almost equal to the Mars rotation period. Consequently, six observations per day can be guaranteed for every Martian day. Reducing the orbital inclination will also be beneficial, even though it may necessitate landing the lander in a narrower belt in lower latitudes. It is recommended that the satellite suitably reduces the altitude and orbital inclination during the mission operations. Once the sampling and returning phases are completed, the orbital inclination could be increased to provide better coverage in high latitudes.

To achieve the scientific objectives of MMC, the selection of wavelengths is essential. Since the MRO MARCI has been a great success, the operation wavelengths of MMC will be similar to those of MARCI. We have decided to design seven channels centered at ~260 nm,

~320 nm, ~425 nm, ~550 nm, ~600 nm, ~770 nm, and ~860 nm, respectively. The expected spatial resolution of the MMC images will be 1 km near nadir points. The images from each channel can be used individually to study various aspects of the Martian atmosphere and surface, such as clouds, circulation, dust swirls and dust storms, atmospheric ozone, surface processes, local albedo properties, surface color properties, mineralogical constraints, and surface physical constraints. These images can also be used to synthesize different channel colors for the identification of Martian dust storms. For example, the false color RGB composite generated from channels at ~425 nm, ~600 nm and ~600 nm could help identify the locations, ranges and evolutions of dust storms, while the false color RGB composite generated from channels at ~260 nm, ~320 nm, and ~425 nm would be suitable for identifying ice clouds thus improving reliability in dust storm identification.

5. Conclusions

Dust storms play a crucial role in the climate system and the space environment of Mars, significantly impacting human Mars exploration activities. The Martian dust storms involve the geological and geochemical processes, surface chemistry and physics, atmospheric chemistry and physics, Mars orbital motion, and solar energy input. Therefore, advancements in understanding the driving mechanisms of Martian dust storms and their environmental effects will promote our understanding of the habitable environment on Mars.

This paper begins by introducing the basic properties, driving mechanisms, and impacts of Martian dust storms. It also provides a brief overview of the history of observing dust storms on Mars while summarizing observation principles and methods for dust storms. Our knowledge of Martian dust storms has advanced considerably through long-term (since the first successful Mars mission) comprehensive observations using spectrometers and cameras as well as simulation efforts.

For the upcoming Tianwen-3 sample return mission, we have statistically predicted the dust activity for potential landing sites. Finally, we proposed an MMC for the Tianwen-3 orbiter to monitor Martian dust storms. The specifications and performance of MMC were simulated to determine that an orbiter altitude of ~300 km with an inclination of ~30° can observe a landing site in the low latitude region during six orbits if its orbital regression period matches the Mars's rotation period. This is critical for the sample return mission as it provides high time resolution monitoring images (~1.76 h) capturing global dust activity on Mars.

At present, the international Mars exploration is in full swing and is expected to enter the era of multi-satellite and multi-lander explorations [155]. In order to conduct an in-depth and systematic study of Martian dust storms, it is essential to establish a stereo observation network in the future that could quantitatively monitor the three-dimensional spatial distribution and dynamic evolution of global dust activities on Mars. To truly understand mechanisms that control the outbreak, development, and decline of dust storms, as well as the interannual variation of global dust storms, missions spanning as many local times and latitudes as possible across the lower, middle, and upper atmosphere are necessary. For orbiters, multicolor cameras and ultraviolet and IR spectrometers will be valuable tools. Small multispectral cameras in visible and near IR bands will be essential for the safe and smooth operation of landers and rovers on Mars.

On the other hand, although models produce dust storms, they do not produce them at the right times and places where such storms are observed without artificial adjustments. The advancement in this field relies on the development of a more comprehensive general circulation model for the whole atmosphere, an improved dust parameterization scheme, and a deeper understanding of dust activities [68]. Observations are the basis for these insights. A stereo observation network would provide a fine climatology, and the attendant monitoring could provide advance notification of dust storms that could impact lander (and aerial) operations. However, a thorough understanding of storm drivers may also necessitate in-situ observations of dust lifting by landers on the surface or laboratory studies focusing on atmospheric dust coagulation and scavenging at far more localized scales.

The proposed MMC will achieve better spatiotemporal resolution for observing dust activity. For specific areas (depending on the orbit of the orbiter), the time resolution of the dust storm image will reach better than 2 h. We can track the onset time of dust storms much more precisely than with day-resolution images. Apart from MMC, a multi-spectral camera will be carried by the lander of the Tianwen-3 mission, which will not only monitor local dust optical depth but also assess the surface property and mineral characteristics near the landing site. The combination of these two instruments will effectively ensure the safe and smooth implementation of the Mars sample return mission. Together with other available observations from instruments, such as MARCI, MCS, ACS, and NOMAD, it is expected that a more comprehensive understanding of the origins and mechanisms behind dust storms will be achieved in future research endeavors.

Author Contributions: Conceptualization, F.H. and Z.R.; methodology, F.H.; software, F.H.; validation, F.H.; formal analysis, F.H.; investigation, F.H., Z.R. and Y.W. (Yong Wei); resources, F.H.; data curation, F.H.; writing—original draft preparation, F.H.; writing—review and editing, F.H., Z.R., Z.W., J.G., K.F., X.Z., L.Y., Y.W. (Yuqi Wang) and Y.W. (Yong Wei); visualization, F.H.; supervision, F.H.; project administration, F.H. and Z.R.; funding acquisition, F.H. and Z.R. All authors have read and agreed to the published version of the manuscript.

Funding: This research was funded by the National Natural Science Foundation of China (42222408, 41931073) and the National Key R&D Program of China (2021YFA0718600). F.H. was supported by the Youth Innovation Promotion Association of the Chinese Academy of Sciences (Y2021027). Z.R. was supported by the Key Research Program of the Chinese Academy of Sciences (ZDBS-SSW-TLC00103) and the Key Research Program of the Institute of Geology and Geophysics, CAS (IGGCAS-202102).

Data Availability Statement: The Opportunity rover's visible dust optical depth data are publicly available at https://pds-geosciences.wustl.edu/mer/mer1_mer2-m-pancam-5-atmos-opacity-v1/merao_1xxx/data/ (accessed on 17 May 2024). The Mars digital elevation map is publicly available at the U.S. Geological Survey Astrogeology Science Center at https://astrogeology.usgs.gov/search/map/Mars/ (accessed on 17 May 2024). The Mars 9.3 μm absorption column dust optical depth database is publicly available at the Mars Climate Database at https://www-mars.lmd.jussieu.fr/mars/dust_climatology/index.html (accessed on 8 March 2023). The Mars Daily Global Maps are publicly available at https://www.msss.com/view.php?page=subject/weather_reports (accessed on 9 March 2024).

Acknowledgments: The authors thank the L. Montabone for providing the Mars dust optical depth database.

Conflicts of Interest: The authors declare no conflicts of interest.

References

1. Connerney, J.E.P.; Acuña, M.H.; Wasilewski, P.J.; Ness, N.F.; Rème, H.; Mazelle, C.; Vignes, D.; Lin, R.P.; Mitchell, D.L.; Cloutier, P.A. Magnetic lineations in the ancient crust of Mars. *Science* **1999**, *284*, 794–798. [CrossRef] [PubMed]
2. Jakosky, B.M. Atmospheric loss to space and the history of water on Mars. *Ann. Rev. Earth Planet. Sci.* **2021**, *49*, 71–93. [CrossRef]
3. Chaffin, M.S.; Kass, D.M.; Aoki, S.; Fedorova, A.A.; Deighan, J.; Connour, K.; Heavens, N.G.; Kleinböhl, A.; Jain, S.K.; Chaufray, J.-Y.; et al. Martian water loss to space enhanced by regional dust storms. *Nat. Astronom.* **2021**, *5*, 1036–1042. [CrossRef]
4. Dubinin, E.; Fraenz, M.; Pätzold, M.; McFadden, J.; Halekas, J.S.; DiBraccio, G.A.; Connerney, J.E.P.; Eparvier, F.; Brain, D.; Jakosky, B.M.; et al. The effect of solar wind variations on the escape of oxygen ions from Mars through different channels: MAVEN observations. *J. Geophys. Res. Space Phys.* **2017**, *122*, 11285–11301. [CrossRef]
5. Heavens, N.G.; Kleinböhl, A.; Chaffin, M.S.; Halekas, J.S.; Kass, D.M.; Hayne, P.O.; McCleese, D.J.; Piqueux, S.; Shirley, J.H.; Schofield, J.T. Hydrogen escape from Mars enhanced by deep convection in dust storms. *Nat. Astronom.* **2018**, *2*, 126–132. [CrossRef]
6. Lillis, R.J.; Brain, D.A.; Bougher, S.W.; Leblanc, F.; Luhmann, J.G.; Jakosky, B.M.; Modolo, R.; Fox, J.; Deighan, J.; Fang, X.; et al. Characterizing atmospheric escape from Mars today and through time, with MAVEN. *Space Sci. Rev.* **2015**, *195*, 357–422. [CrossRef]

7. Lundin, R.; Barabash, S.; Andersson, H.; Holmström, M.; Grigoriev, A.; Yamauchi, M.; Sauvaud, J.-A.; Fedorov, A.; Dudnik, E.; Thocaven, J.J.; et al. Solar wind-induced atmospheric erosion at Mars: First results from ASPERA-3 on Mars Express. *Science* **2004**, *305*, 1933–1936. [CrossRef]
8. Ramstad, R.; Barabash, S.; Futaana, Y.; Nilsson, H.; Wang, X.-D.; Holmström, M. The Martian atmospheric ion escape rate dependence on solar wind and solar EUV conditions: 1. Seven years of Mars Express observations. *J. Geophys. Res. Planets* **2015**, *120*, 1298–1309. [CrossRef]
9. Wei, Y.; Fraenz, M.; Dubinin, E.; Woch, J.; Lühr, H.; Wan, W.; Zong, Q.-G.; Zhang, T.L.; Pu, Z.Y.; Fu, S.Y.; et al. Enhanced atmospheric oxygen outflow on Earth and Mars driven by a corotating interaction region. *J. Geophys. Res.* **2012**, *117*, A03208. [CrossRef]
10. Barlow, N. *Mars: An Introduction to Its Interior, Surface and Atmosphere*; Cambridge University Press: New York, NY, USA, 2008; pp. 163–186.
11. Leovy, C. Weather and climate on Mars. *Nature* **2001**, *412*, 245–249. [CrossRef]
12. Shirley, J.H. Solar system dynamics and global-scale dust storms on Mars. *Icarus* **2015**, *251*, 128–144. [CrossRef]
13. Keiffer, H.H.; Jakosky, B.M.; Snyder, C.W.; Matthews, M.S. *Mars*; Univ. Ariz. Press: Tucson, AZ, USA, 1992.
14. Haberle, R.M.; Clancy, R.T.; Forget, F.; Smith, M.D.; Zurek, R.W. *The Atmosphere and Climate of Mars*; Cambridge University Press: New York, NY, USA, 2007.
15. Encrenaz, T. The atmosphere of Mars as constrained by remote sensing. *Space Sci. Rev.* **2001**, *96*, 411–424. [CrossRef]
16. Smith, M.D. Spacecraft observations of Martian atmosphere. *Ann. Rev. Earth Planet. Sci.* **2008**, *36*, 191–219. [CrossRef]
17. Schmidt, F.; Way, M.J.; Costard, F.; Bouley, S.; Séjourné, A.; Aleinov, I. Circumpolar ocean stability on Mars 3 Gy ago. *Proc. Natl. Acad. Sci. USA* **2022**, *119*, e2112930118. [CrossRef] [PubMed]
18. Wei, Y.; He, F.; Fan, K.; Rong, Z.; Wang, Y. Preliminary predictions of the dust storm activity at the landing site of China’s Zhurong Mars rover in 2022. *Chin. Sci. Bull.* **2022**, *67*, 1938–1944. (In Chinese) [CrossRef]
19. Wang, Y.; Wei, Y.; Fan, K.; He, F.; Rong, Z.; Zhou, X.; Tan, N. The impact of dust storms on Mars surface rovers: Review and prospect. *Chin. Sci. Bull.* **2023**, *68*, 368–379. (In Chinese) [CrossRef]
20. Rong, Z.; Wei, Y.; He, F.; Gao, J.; Fan, K.; Wang, Y.; Cao, L.; Yan, L.; Ren, Z.; Zhou, X.; et al. The orbit schemes to monitor Martian dust storms: Benefits to China’s future mars missions. *Chin. Sci. Bull.* **2023**, *68*, 716–728. (In Chinese) [CrossRef]
21. James, P.B. Martian local dust storms. In *Recent Advances in Planetary Meteorology*; Hunt, G., Ed.; Cambridge University Press: New York, NY, USA, 1985; pp. 85–100.
22. Martin, L.J.; Zurek, R.W. An analysis of the history of dust activity on Mars. *J. Geophys. Res.* **1993**, *98*, 3221–3246. [CrossRef]
23. Zurek, R.W.; Martin, L.J. Interannual variability of planet-encircling dust storms on Mars. *J. Geophys. Res.* **1993**, *98*, 3247–3259. [CrossRef]
24. Fernández, W. Martian dust storms: A review. *Earth Moon Planet.* **1997**, *77*, 19–46. [CrossRef]
25. Kahre, M.A.; Murphy, J.R.; Newman, C.E.; Wilson, R.J.; Cantor, B.A.; Lemmon, M.T.; Wolff, M.J. The Mars Dust Cycle. In *The Atmosphere and Climate of Mars*; Haberle, R.M., Clancy, R.T., Forget, F., Smith, M.D., Zurek, R.W., Eds.; Cambridge University Press: New York, NY, USA, 2007; pp. 295–337.
26. Malin, M.C.; Cantor, B.A. MRO MARCI Weather Report for the week of 27 December 2021–2 January 2022. Malin Space Science Systems Captioned Image Release, 2022, MSSS-603. Available online: https://www.msss.com/msss_images/2022/01/05/ (accessed on 9 March 2024).
27. Malin, M.C.; Cantor, B.A.; Britton, A.W. MRO MARCI Weather Report for the week of 4 June 2018–10 June 2018, Malin Space Science Systems Captioned Image Release, 2018, MSSS-534. Available online: https://www.msss.com/msss_images/2018/06/13/ (accessed on 9 March 2024).
28. Cantor, B.A.; James, P.B.; Caplinger, M.; Wolff, M.J. Martian dust storms: 1999 Mars Orbiter Camera observations. *J. Geophys. Res.* **2001**, *106*, 23653–23688. [CrossRef]
29. Wang, H.; Richardson, M.I. The origin, evolution, and trajectory of large dust storms on Mars during Mars Year 24–30 (1999–2011). *Icarus* **2015**, *251*, 112–127. [CrossRef]
30. Kulowski, L.; Wang, H.; Toigo, A.D. The seasonal and spatial distribution of textured dust storms observed by Mars Global Surveyor Mars Orbiter Camera. *Adv. Space Res.* **2017**, *59*, 715–721. [CrossRef]
31. Guzewich, S.D.; Fedorova, A.A.; Kahre, M.A.; Toigo, A.D. Studies of the 2018/Mars Year 34 planet-encircling dust storm. *J. Geophys. Res. Planets* **2020**, *125*, e2020JE006700. [CrossRef]
32. Wang, H.; Saidel, M.; Richardson, M.I.; Toigo, A.D.; Battalio, J.M. Martian dust storm distribution and annual cycle from Mars daily global map observations. *Icarus* **2023**, *394*, 115416. [CrossRef]
33. Sánchez-Lavega, A.; del Río-Gaztelurrutia, T.; Hernández-Bernal, J.; Delcroix, M. The onset and growth of the 2018 Martian Global Dust Storm. *Geophys. Res. Lett.* **2019**, *46*, 6101–6108. [CrossRef]
34. Kass, D.M.; Kleinböhl, A.; McCleese, D.J.; Schofield, J.T.; Smith, M.D. Interannual similarity in the Martian atmosphere during the dust storm season. *Geophys. Res. Lett.* **2016**, *43*, 6111–6118. [CrossRef]
35. Montabone, L.; Forget, F.; Millour, E.; Wilson, R.J.; Lewis, S.R.; Cantor, B.; Kass, D.; Kleinböhl, A.; Lemmon, M.T.; Smith, M.D.; et al. Eight-year climatology of dust optical depth on Mars. *Icarus* **2015**, *251*, 65–95. [CrossRef]

36. Montabone, L.; Spiga, A.; Kass, D.M.; Kleinböhl, A.; Forget, F.; Millour, E. Martian year 34 column dust climatology from Mars Climate Sounder observations: Reconstructed maps and model simulations. *J. Geophys. Res. Planets* **2020**, *125*, e2019JE006111. [CrossRef]
37. Lemmon, M.T.; Guzewich, S.D.; McConnochie, T.; de Vicente-Retortillo, A.; Martínez, G.; Smith, M.D.; Bell, J.F., III; Wellington, D.; Jacob, S. Large dust aerosol sizes seen during the 2018 Martian global dust event by the Curiosity rover. *Geophys. Res. Lett.* **2019**, *46*, 9448–9456. [CrossRef]
38. Chen-Chen, H.; Pérez-Hoyos, S.; Sánchez-Lavega, A. Dust particle size, shape and optical depth during the 2018/MY34 Martian global dust storm retrieved by MSL Curiosity rover Navigation Cameras. *Icarus* **2021**, *354*, 114021. [CrossRef]
39. Clancy, R.T.; Wolff, M.J.; Christensen, P.R. Mars aerosol studies with the MGS TES emission phase function observations: Optical depths, particle sizes, and ice cloud types versus latitude and solar longitude. *J. Geophys. Res.* **2003**, *108*, 5098. [CrossRef]
40. Wolff, M.J.; Clancy, R.T. Constraints on the size of Martian aerosols from thermal emission spectrometer observations. *J. Geophys. Res.* **2003**, *108*, 5097. [CrossRef]
41. Vicente-Retortillo, Á.; Martínez, G.; Rennó, N.; Lemmon, M.T.; de la Torre Juarez, M. Determination of dust aerosol particle size at Gale crater using REMS UVS and Mastcam measurements. *Geophys. Res. Lett.* **2017**, *44*, 3502–3508. [CrossRef]
42. Fedorova, A.A.; Montmessin, F.; Rodin, A.V.; Korablev, O.I.; Maattanen, A.; Maltagliati, L.; Bertaux, J.-L. Evidence for a bimodal size distribution for the suspended aerosol particles on Mars. *Icarus* **2014**, *231*, 239–260. [CrossRef]
43. Bertaux, J.-L.; Korablev, O.; Perrier, S.; Quémerais, E.; Montmessin, F.; Leblanc, F.; Lebonnois, S.; Rannou, P.; Lefèvre, F.; Forget, F.; et al. SPICAM on Mars Express: Observing modes and overview of UV spectrometer data and scientific results. *J. Geophys. Res.* **2006**, *111*, E10S90. [CrossRef]
44. Guzewich, S.D.; Tiogo, A.D.; Richardson, M.I.; Newman, C.E.; Talaat, E.R.; Waugh, D.W.; McConnochie, T.H. The impact of a realistic vertical dust distribution on the simulation of the Martian General Circulation. *J. Geophys. Res. Planet.* **2013**, *118*, 980–993. [CrossRef]
45. Medvedev, A.S.; Yiğit, E.; Kuroda, T.; Hartogh, P. General circulation modeling of the Martian upper atmosphere during global dust storms. *J. Geophys. Res. Planet.* **2013**, *118*, 2234–2246. [CrossRef]
46. Wang, Y.; Chow, K.-C.; Xiao, J.; Wang, C.-F. Effect of dust particle size on the climate of Mars. *Planet. Space Sci.* **2021**, *208*, 105346. [CrossRef]
47. Hanel, R.; Conrath, B.; Hovis, W.; Kunde, V.; Lowman, P.; Maguire, W.; Pearl, J.; Pirraglia, J.; Prabhakara, C.; Schlachman, B.; et al. Investigation of the Martian environment by infrared spectroscopy on Mariner 9. *Icarus* **1972**, *17*, 423–442. [CrossRef]
48. Leovy, C.B.; Zurek, R.W.; Pollack, J.B. Mechanisms for Mars dust storms. *J. Atmos. Sci.* **1973**, *30*, 749–762. [CrossRef]
49. Gierasch, P.J.; Goody, R.M. A model of a Martian great dust storm. *J. Atmos. Sci.* **1973**, *30*, 169–179. [CrossRef]
50. Leovy, C.B.; Briggs, G.A.; Young, A.T.; Smith, B.A.; Pollack, J.B.; Shipley, E.N.; Wildey, R.L. The Martian atmosphere: Mariner 9 television experiment progress report. *Icarus* **1972**, *17*, 373–393. [CrossRef]
51. Cross, C.A. The heat balance of the Martian polar caps. *Icarus* **1971**, *15*, 110–114. [CrossRef]
52. Ryan, J.A.; Sharman, R.D.; Lucich, R.D. Local Mars dust storm generation mechanism. *Geophys. Res. Lett.* **1981**, *8*, 899–901. [CrossRef]
53. Ryan, J.A.; Lucich, R.D. Possible dust devils, vortices on Mars. *J. Geophys. Res.* **1983**, *88*, 11005–11011. [CrossRef]
54. Hess, S.L. Martian winds and dust clouds. *Planet. Space Sci.* **1973**, *21*, 1549–1557. [CrossRef]
55. Newman, C.E.; Lewis, S.R.; Read, S.R.; Forget, F. Modeling the Martian dust cycle, 1, Representations of dust transport processes. *J. Geophys. Res.* **2002**, *107*, 5123. [CrossRef]
56. Newman, C.E.; Lewis, S.R.; Read, S.R.; Forget, F. Modeling the Martian dust cycle, 2, Multiannual radiatively active dust transport simulations. *J. Geophys. Res.* **2002**, *107*, 5124. [CrossRef]
57. Basu, S.; Wilson, J.; Richardson, M.; Ingersoll, A. Simulation of spontaneous and variable global dust storms with the GFDL Mars GCM. *J. Geophys. Res.* **2006**, *111*, E09004. [CrossRef]
58. Kahre, M.A.; Murphy, J.R.; Haberle, R.M. Modeling the Martian dust cycle and surface dust reservoirs with the NASA Ames general circulation model. *J. Geophys. Res.* **2006**, *11*, E06008. [CrossRef]
59. Xiao, J.; Chow, K.C.; Chan, K. Dynamical processes of dust lifting in the northern mid-latitude region of Mars during the dust storm season. *Icarus* **2019**, *317*, 94–103. [CrossRef]
60. Forget, F.; Hourdin, F.; Fournier, R.; Hourdin, C.; Talagrand, O.; Collins, M.; Lewis, S.R.; Read, P.L.; Huot, J.P. Improved general circulation model for the Martian atmosphere from the surface to above 80 km. *J. Geophys. Res.* **1999**, *104*, 24155–24175. [CrossRef]
61. Petrosyan, A.; Galperin, B.; Larsen, S.E.; Lewis, S.R.; Määttänen, A.; Read, P.L.; Renno, N.; Rogberg, L.P.H.T.; Savijärvi, H.; Siili, T.; et al. The Martian atmospheric boundary layer. *Rev. Geophys.* **2011**, *49*, RG3005. [CrossRef]
62. Shirley, J.H.; Mischna, M.A. Orbit-spin coupling and the interannual variability of global-scale dust storm occurrence on Mars. *Planet. Space Sci.* **2017**, *139*, 37–50. [CrossRef]
63. Mischna, M.A.; Shirley, J.H. Numerical modeling of orbit-spin coupling accelerations in a Mars general circulation model: Implications for global dust storm activity. *Planet. Space Sci.* **2017**, *141*, 45–72. [CrossRef]
64. Newman, C.E.; Lee, C.; Mischna, M.A.; Richardson, M.I.; Shirley, J.H. An initial assessment of the impact of postulated orbit-spin coupling on Mars dust storm variability in fully interactive dust simulations. *Icarus* **2019**, *317*, 649–668. [CrossRef]
65. Shirley, J.H.; McKim, R.J.; Battalio, J.M.; Kass, D.M. Orbit-Spin Coupling and the Triggering of the Martian Planet-Encircling Dust Storm of 2018. *J. Geophys. Res. Planets* **2020**, *125*, e2019JE006077. [CrossRef]

66. Bertrand, T.; Wilson, R.J.; Kahre, M.A.; Urata, R.; Kling, A. Simulation of the 2018 global dust storm on Mars using the NASA Ames Mars GCM: A multitracer approach. *J. Geophys. Res. Planets* **2020**, *125*, e2019JE006122. [CrossRef]
67. Wu, Z.; Li, T.; Heavens, N.G.; Newman, C.E.; Richardson, M.I.; Yang, C.; Li, J.; Cui, J. Earth-like thermal and dynamical coupling processes in the Martian climate system. *Earth Sci. Rev.* **2022**, *229*, 104023. [CrossRef]
68. Zhou, X.; Wei, Y.; Wu, Z.; Ren, Z.; Tan, N.; Fan, S.; He, F.; Rong, Z.; Yan, L.; Wang, Y.; et al. Martian whole atmosphere model and dust activities: Review and prospect. *Chin. Sci. Bull.* **2024**, *69*, 1058–1067. (In Chinese) [CrossRef]
69. Fenton, L.K.; Geissler, P.E.; Haberle, R.M. Global warming and climate forcing by recent albedo changes on Mars. *Nature* **2007**, *446*, 646–649. [CrossRef]
70. Kass, D.M.; Schofield, J.T.; Kleinböhl, A.; McCleese, D.J.; Heavens, N.G.; Shirley, J.H.; Steele, L.J. Mars Climate Sounder observation of Mars' 2018 global dust storm. *Geophys. Res. Lett.* **2020**, *47*, e2019GL083931. [CrossRef]
71. Guzewich, S.D.; Lemmon, M.; Smith, C.L.; Martínez, G.; de Vicente-Retortillo, Á.; Newman, C.E.; Baker, M.; Campbell, C.; Cooper, B.; Gómez-Elvira, J.; et al. Mars Science Laboratory observations of the 2018/Mars year 34 global dust storm. *Geophys. Res. Lett.* **2019**, *46*, 71–79. [CrossRef]
72. Haberle, R.M.; Pollack, J.B.; Barnes, J.R.; Zurek, R.W.; Leovy, C.B.; Murphy, J.R.; Lee, H.; Schaeffer, J. Mars atmospheric dynamics as simulated by the NASA Ames General Circulation Model: 1. The zonal-mean circulation. *J. Geophys. Res.* **1993**, *98*, 3093–3123. [CrossRef]
73. Wu, Z.; Li, T.; Zhang, X.; Li, J.; Cui, J. Dust tides and rapid meridional motions in the Martian atmosphere during major dust storms. *Nat. Commun.* **2020**, *11*, 614. [CrossRef] [PubMed]
74. Zhao, Y.; Zhong, L.; Yuan, R.; Zhao, C.; Li, R.; Wang, Y.; Lian, Y.; Richardson, M. Simulation of Martian dust effects on polar CO_2 ice caps and atmospheric circulation using the MarsWRF model. *J. Geophys. Res. Planet.* **2021**, *126*, e2021JE006937. [CrossRef]
75. Melnik, O.; Parrot, M. Electrostatic discharge in Martian dust storms. *J. Geophys. Res.* **1998**, *103*, 29107–29117. [CrossRef]
76. Farrell, W.M.; Kaiser, M.L.; Desch, M.D.; Houser, J.G.; Cummer, S.A.; Wilt, D.M.; Landis, G.A. Detecting electrical activity from Martian dust storms. *J. Geophys. Res.* **1999**, *104*, 3795–3801. [CrossRef]
77. Krauss, C.E.; Horanyi, M.; Robertson, S. Experimental evidence for electrostatic discharging of dust near the surface of Mars. *New J. Phys.* **2003**, *5*, 70. [CrossRef]
78. Merrison, J.; Jensen, J.; Kinch, K.; Mugford, R.; Nørnberg, P. The electrical properties of Mars analogue dust. *Planet Space Sci.* **2004**, *52*, 279–290. [CrossRef]
79. Michael, M.; Tripathi, S.N. Effect of charging of aerosols in the lower atmosphere of Mars during the dust storm of 2001. *Planet Space Sci.* **2008**, *56*, 1696–1702. [CrossRef]
80. Haider, S.A.; Sheel, V.; Smith, M.D.; Maguire, W.C.; Molina-Cuberos, G.J. Effect of dust storms on the D region of the Martian ionosphere: Atmospheric electricity. *J. Geophys. Res. Space Phys.* **2010**, *115*, A12336. [CrossRef]
81. McDunn, T.L.; Bougher, S.W.; Murphy, J.; Smith, M.D.; Forget, F.; Bertaux, J.-L.; Montmessin, F. Simulating the density and thermal structure of the middle atmosphere (80–130 km) of Mars using the MGCM–MTGCM: A comparison with MEX/SPICAM observations. *Icarus* **2010**, *206*, 5–17. [CrossRef]
82. Chaufray, J.Y.; Chaffin, M.S.; Deighan, J.; Jain, S.; Schneider, N.; Mayyasi, M.; Jakosky, B. Effect of the 2018 Martian global dust storm on the CO2 density in the lower nightside thermosphere observed from MAVEN/IUVS Lyman-alpha absorption. *Geophys. Res. Lett.* **2020**, *47*, e2019GL082889. [CrossRef]
83. Fang, X.; Ma, Y.; Lee, Y.; Bougher, S.; Liu, G.; Benna, M.; Mahaffy, P.; Montabone, L.; Pawlowski, D.; Dong, C.; et al. Mars dust storm effects in the ionosphere and magnetosphere and implications for atmospheric carbon loss. *J. Geophys. Res. Space Phys.* **2020**, *125*, e2019JA026838. [CrossRef]
84. Niu, D.D.; Cui, J.; Wu, S.Q.; Gu, H.; Cao, Y.-T.; Wu, Z.-P.; Wu, X.-S.; Zhong, J.-H.; Wu, M.-Y.; Wei, Y.; et al. Species-dependent response of the Martian ionosphere to the 2018 global dust event. *J. Geophys. Res. Planets* **2021**, *126*, e2020JE006679. [CrossRef]
85. Mukundan, V.; Thampi, S.V.; Bhardwaj, A.; Fang, X. Impact of the 2018 Mars global dust storm on the ionospheric peak: A study using a photochemical model. *J. Geophys. Res. Planets* **2021**, *126*, e2021JE006823. [CrossRef]
86. Stone, S.W.; Yelle, R.V.; Benna, M.; Lo, D.Y.; Elrod, M.K.; Mahaffy, P.R. Hydrogen escape from Mars is driven by seasonal and dust storm transport of water. *Science* **2020**, *370*, 824–831. [CrossRef]
87. Clancy, R.T.; Nair, H. Annual (perihelion-aphelion) cycles in the photochemical behavior of the global Mars atmosphere. *J. Geophys. Res. Planets* **1996**, *101*, 12785–12790. [CrossRef]
88. Clancy, R.T.; Wolff, M.J.; Lefèvre, F.; Cantor, B.A.; Malin, M.C.; Smith, M.D. Daily global mapping of Mars ozone column abundances with MARCI UV band imaging. *Icarus* **2016**, *266*, 112–133. [CrossRef]
89. Hvidberg, C.S.; Fishbaugh, K.E.; Winstrup, M.; Svensson, A.; Byrne, S.; Herkenhoff, K.E. Reading the climate record of the Martian polar layered deposits. *Icarus* **2012**, *221*, 405–419. [CrossRef]
90. Colaprete, A.; Barnes, J.; Haberle, R.; Hollingsworth, J.L.; Kieffer, H.H.; Titus, T.N. Albedo of the south pole on Mars determined by topographic forcing of atmosphere dynamics. *Nature* **2005**, *435*, 184–188. [CrossRef] [PubMed]
91. Golombek, M.P.; Warner, N.H.; Ganti, V.; Lamb, M.P.; Parker, T.J.; Fergason, R.L.; Sullivan, R. Small crater modification on Meridiani Planum and implications for erosion rates and climate change on Mars. *J. Geophys. Res. Planets* **2014**, *119*, 2522–2547. [CrossRef]

92. Farley, K.A.; Malespin, C.; Mahaffy, P.; Grotzinger, J.P.; Vasconcelos, P.M.; Milliken, R.E.; Malin, M.; Edgett, K.S.; Pavlov, A.A.; Hurowitz, J.A.; et al. In Situ Radiometric and Exposure Age Dating of the Martian Surface. *Science* **2013**, *343*, 1247166. [CrossRef] [PubMed]
93. Vasavada, A.R.; Chen, A.; Barnes, J.R.; Burkhart, P.D.; Cantor, B.A.; Dwyer-Cianciolo, A.M.; Fergason, R.L.; Hinson, D.P.; Justh, H.L.; Kass, D.M.; et al. Assessment of environments for mars science laboratory entry, descent, and surface operations. *Space Sci. Rev.* **2012**, *170*, 793–835. [CrossRef]
94. Team, R. Characterization of the Martian Surface Deposits by the Mars Pathfinder Rover, Sojourner. *Science* **1997**, *278*, 1765–1767. [CrossRef]
95. Rieder, R.T.; Economou, T.E.; Wänke, H.; Turkevich, A.; Crisp, J.; Brückner, J.; Dreibus, G.; McSween, H.Y., Jr. The Chemical Composition of Martian Soil and Rocks Returned by the Mobile Alpha Proton X-ray Spectrometer: Preliminary Results from the X-ray Mode. *Science* **1998**, *278*, 1771–1774. [CrossRef]
96. Lorenz, R.D.; Martínez, G.M.; Spiga, A.; Vicente-Retortillo, A.; Newman, C.E.; Murdoch, N.; Forget, F.; Millour, E.; Pierron, T. Lander and rover histories of dust accumulation on and removal from solar arrays on Mars. *Planet. Space Sci.* **2021**, *207*, 105337. [CrossRef]
97. Landis, G.A.; Jenkins, P.P. Measurement of the settling rate of atmospheric dust on Mars by the MAE instrument on Mars Pathfinder. *J. Geophys. Res.* **2000**, *105*, 1855–1857. [CrossRef]
98. Crisp, D.; Pathare, A.; Ewell, R.C. The performance of gallium arsenide/germanium solar cells at the Martian surface. *Acta Astronaut.* **2004**, *54*, 83–101. [CrossRef]
99. Staab, M.S.; Herman, J.A.; Reich, K.; Reich, K.; Sridhar, V.; Nelson, R.W. MER Opportunity dust-storm recovery operations and implications for future Mars surface missions. In Proceedings of the 2020 IEEE Aerospace Conference, Big Sky, MT, USA, 7–14 March 2020.
100. Yen, A.; Gellert, R.; Schröder, C.; Morris, R.V.; Bell, J.F., III; Knudson, A.T.; Clark, B.C.; Ming, D.M.; Crisp, J.A.; Arvidson, R.E.; et al. An integrated view of the chemistry and mineralogy of Martian soils. *Nature* **2005**, *436*, 49–54. [CrossRef] [PubMed]
101. Slipher, E.C. *Mars—The Photographic Story*; Northland Press: Flagstaff, AZ, USA, 1962.
102. Horn, D.; McAfee, J.M.; Winer, A.M.; Herr, K.C.; Pimentel, G.C. The composition of the Martian atmosphere: Minor constituents. *Icarus* **1972**, *16*, 543–556. [CrossRef]
103. Cimino, G.; Clavin, W.M. Calibration and analysis of Mariner 7 infrared spectra. *Bull. Am. Astron. Soc.* **1996**, *28*, 1068.
104. Hord, C.W.; Barth, C.A.; Stewart, A.I.; Lane, A.L. Mariner 9 ultraviolet spectrometer experiment: Photometry and topography of Mars. *Icarus* **1972**, *17*, 433–456. [CrossRef]
105. Anderson, E.; Loevy, C. Mariner 9 television limb observations of dust and ice hazes on Mars. *J. Atmos. Sci.* **1978**, *35*, 723. [CrossRef]
106. Martin, T.Z.; Richardson, M.I. New dust opacity mapping from Viking infrared thermal mapper data. *J. Geophys. Res.* **1993**, *98*, 10941–10949. [CrossRef]
107. Biggs, G.A.; Baum, W.A.; Barnes, J. Viking Orbiter imaging observations of dust in the martian atmosphere. *J. Geophys. Res.* **1979**, *84*, 2795. [CrossRef]
108. Malin, M.C.; Danielson, G.E.; Ravine, M.A.; Soulanille, T.A. Design and development of the Mars Observer Camera. *Int. J. Imaging Syst. Technol.* **1991**, *3*, 76–91. [CrossRef]
109. Malin, M.C.; Danielson, G.E.; Ingersoll, A.P.; Masursky, H.; Veverka, J.; Ravine, M.A.; Soulanille, T.A. Mars Observer Camera. *J. Geophys. Res.* **1992**, *97*, 7699–7718. [CrossRef]
110. Christensen, P.R.; Bandfield, J.L.; Hamilton, V.E.; Ruff, S.W.; Kieffer, H.H.; Titus, T.N.; Malin, M.C.; Morris, R.V.; Lane, M.D.; Clark, R.L.; et al. Mars Global Surveyor Thermal Emission Spectrometer experiment: Investigation description and surface science results. *J. Geophys. Res.* **2001**, *106*, 23823–23871. [CrossRef]
111. Tomasko, M.G.; Doose, L.R.; Lemmon, M.; Smith, P.H.; Wegryn, E. Properties of dust in Martian atmosphere from the Imager on Mars Pathfinder. *J. Geophys. Res.* **1999**, *104*, 8987–9007. [CrossRef]
112. Smith, P.H.; Lemmon, M. Opacity of the Martian atmosphere measured by the Imager for Mars Pathfinder. *J. Geophys. Res.* **1999**, *104*, 8975–8985. [CrossRef]
113. Christensen, P.R.; Jakosky, B.M.; Kieffer, H.H.; Malin, M.C.; McSween, H.Y., Jr.; Nealson, K.; Mehall, G.L.; Silverman, S.H.; Ferry, S.; Caplinger, M.; et al. The Thermal Emission Imaging System (THEMIS) for the Mars 2001 Odyssey mission. *Space Sci. Rev.* **2004**, *110*, 85–130. [CrossRef]
114. Määttänen, A.; Listowski, C.; Montmessin, F.; Maltagliati, L.; Reberac, A.; Joly, L.; Bertaux, L.J. A complete climatology of the aerosol vertical distribution on Mars from MEx/SPICAM UV solar occultations. *Icarus* **2013**, *223*, 892–941. [CrossRef]
115. Bibring, J.-P.; Soufflot, A.; Berthé, M.; Langevin, Y.; Gondet, B.; Drossart, P.; Bouyé, M.; Combes, M.; Puget, P.; Semery, A.; et al. OMEGA: Observatoire pour la Mineralogie, l'Eau, les Glaces et l'Activité. *Eur. Space Agency Spec. Pub.* **2004**, *1240*, 37.
116. Gwinner, K.; Jaumann, R.; Hauber, E.; Hoffmann, H.; Heipke, C.; Oberst, J.; Neukum, G.; Ansan, V.; Bostelmann, J.; Dumke, A.; et al. The High Resolution Stereo Camera (HRSC) of Mars Express and its approach to science analysis and mapping for Mars and its satellites. *Planet. Space Sci.* **2016**, *126*, 93–138. [CrossRef]
117. Lemmon, M.T.; Wolff, M.J.; Bell, J.F., III; Smith, M.D.; Cantor, B.A.; Smith, P.H. Dust aerosol, clouds, and the atmospheric optical depth record over 5 Mars years of the Mars Exploration Rover mission. *Icarus* **2015**, *251*, 96–111. [CrossRef]

118. Bell, J.F., III; Squyres, S.W.; Herkenhoff, K.E.; Maki, J.N.; Arneson, H.M.; Brown, D.; Collins, S.A.; Dingizian, A.; Elliot, S.T.; Hagerott, E.C.; et al. Mars Exploration Rover Athena Panoramic Camera (Pancam) investigation. *J. Geophys. Res. Planets* **2003**, *108*, 8063. [CrossRef]
119. Chistensen, P.R.; Mehall, G.L.; Silverman, S.H.; Anwar, S.; Cannon, G.; Gorelick, N.; Kheen, R.; Tourville, T.; Bates, D.; Ferry, S.; et al. Miniature Thermal Emission Spectrometer for the Mars Exploration Rovers. *J. Geophys. Res. Planets* **2003**, *108*, 8064.
120. Bell, J.F., III; Wolff, M.J.; Malin, M.C.; Calvin, W.M.; Cantor, B.A.; Caplinger, M.A.; Clancy, R.T.; Edgett, K.S.; Edwards, L.J.; Fahle, J.; et al. Mars Reconnaissance Orbiter Mars Color Imager (MARCI): Instrument description, calibration, and performance. *J. Geophys. Res. Planets* **2009**, *114*, E08S92. [CrossRef]
121. Murchie, S.; Arvidson, R.; Bedini, P.; Beisser, K.; Bibring, J.-P.; Bishop, J.; Boldt, J.; Cavender, P.; Choo, T.; Clancy, R.T.; et al. Compact Reconnaissance Imaging Spectrometer for Mars (CRISM) on Mars Reconnaissance Orbiter (MRO). *J. Geophys. Res. Planets* **2007**, *112*, E05S03. [CrossRef]
122. McCleese, D.J.; Schofield, J.T.; Taylor, F.W.; Calcutt, S.B.; Foote, M.C.; Kass, D.M.; Leovy, C.B.; Paige, D.A.; Read, P.L.; Zurek, R.W. Mars Climate Sounder: An investigation of thermal and water vapor structure, dust and condensate distributions in the atmosphere, and energy balance of the polar regions. *J. Geophys. Res. Planets* **2007**, *112*, E05S06. [CrossRef]
123. Smith, P.H.; Tamppari, L.; Arvidson, R.E.; Bass, D.; Blaney, D.; Boynton, W.; Carswell, A.; Catling, D.; Clark, B.; Duck, T.; et al. Introduction to special section on the Phoenix Mission: Landing Site Characterization Experiments, Mission Overviews, and Expected Science. *J. Geophys. Res. Planets* **2008**, *113*, E00A18. [CrossRef]
124. Grotzinger, J.P.; Crisp, J.; Vasavada, A.R.; Anderson, R.C.; Baker, C.J.; Barry, R.; Blake, D.F.; Conrad, P.; Edgett, K.S.; Ferdowski, B.; et al. Mars Science Laboratory mission and science investigation. *Space Sci. Rev.* **2012**, *170*, 5–56. [CrossRef]
125. Vandaele, A.C.; Neefs, E.; Drummond, R.; Thomas, I.R.; Daerden, F.; Lopez-Moreno, J.-J.; Rodriguez, J.; Patel, M.R.; Bellucci, G.; Allen, M.; et al. Science objectives and performances of NOMAD, a spectrometer suite for the ExoMars TGO mission. *Planet. Space Sci.* **2015**, *119*, 233–249. [CrossRef]
126. Thomas, N.; Cremonese, G.; Ziethe, R.; Gerber, M.; Brändli, M.; Bruno, G.; Erismann, M.; Gambicorti, L.; Gerber, T.; Ghose, K.; et al. The Colour and Stereo Surface Imaging System (CaSSIS) for the ExoMars Trace Gas Orbiter. *Space Sci. Rev.* **2017**, *212*, 1897–1944. [CrossRef]
127. Korablev, O.; Montmessin, F.; Trokhimovskiy, A.; Fedorova, A.A.; Shakun, A.V.; Grigoriev, A.V.; Moshkin, B.E.; Ignatiev, N.I.; Forget, F.; Lefèvre, F.; et al. The Atmospheric Chemistry Suite (ACS) of Three Spectrometers for the ExoMars 2016 Trace Gas Orbiter. *Space Sci. Rev.* **2018**, *214*, 7. [CrossRef]
128. Maki, J.N.; Golombek, M.; Deen, R.; Abarca, H.; Sorice, C.; Goodsall, T.; Schwochert, M.; Lemmon, M.; Trebi-Ollennu, A.; Banerdt, W.B. The Color Cameras on the InSight Lander. *Space Sci. Rev.* **2018**, *214*, 105. [CrossRef]
129. Banfield, D.; Rodriguez-Manfredi, J.A.; Russell, C.T.; Rowe, K.M.; Leneman, D.; Lai, H.R.; Cruce, P.R.; Means, J.D.; Johnson, C.L.; Mittelholz, A.; et al. Insight Auxiliary Payload Sensor Suite (APSS). *Space Sci. Rev.* **2019**, *215*, 4. [CrossRef]
130. Bell, J.F., III; Maki, J.N.; Mehall, G.L.; Ravine, M.A.; Caplinger, M.A.; Bailey, Z.J.; Brylow, S.; Schaffner, J.A.; Kinch, K.M.; Madsen, M.B.; et al. The Mars 2020 Perseverance Rover Mast Camera Zoom (Mastcam-Z) Multispectral, Stereoscopic Imaging Investigation. *Space Sci. Rev.* **2021**, *217*, 24. [CrossRef]
131. Maurice, S.; Wiens, R.C.; Bernardi, P.; Caïs, P.; Robinson, S.; Nelson, T.; Gasnault, O.; Reess, J.-M.; Deleuze, M.; Rull, F.; et al. The SuperCam Instrument Suite on the Mars 2020 Rover: Science Objectives and Mast-Unit Description. *Space Sci. Rev.* **2021**, *217*, 47. [CrossRef]
132. Rodriguez-Manfredi, J.A.; de la Torre Juárez, M.; Alonso, A.; Apéstigue, V.; Arruego, I.; Atienza, T.; Banfield, D.; Boland, J.; Carrera, M.A.; Castañer, L.; et al. The Mars Environmental Dynamics Analyzer, MEDA. A Suite of Environmental Sensors for the Mars 2020 Mission. *Space Sci. Rev.* **2021**, *217*, 48. [CrossRef] [PubMed]
133. Jones, A.R.; Wolff, M.; Alshamsi, M.; Osterloo, M.; Bay, P.; Brennan, N.; Bryant, K.; Castleman, Z.; Curtin, A.; DeVito, E.; et al. The Emirates Exploration Imager (EXI) Instrument on the Emirates Mars Mission (EMM) Hope Mission. *Space Sci. Rev.* **2021**, *217*, 81. [CrossRef]
134. Meng, Q.; Wang, D.; Wang, X.; Li, W.; Yang, X.; Yan, D.; Li, Y.; Cao, Z.; Ji, Q.; Sun, T.; et al. High Resolution Imaging Camera (HiRiC) on China's first Mars exploration Tianwen-1 mission. *Space Sci. Rev.* **2021**, *217*, 42. [CrossRef]
135. Yu, G.B.; Liu, E.H.; Liu, G.L.; Zhou, L.; Zeng, J.Z.; Chen, Y.P.; Zhou, X.D.; Zhao, R.J.; Zhu, S.Y. Moderate Resolution Imaging Camera (MoRIC) of China's First Mars Mission Tianwen-1. *Earth Planet. Phys.* **2020**, *4*, 364–370. [CrossRef]
136. Yang, J.-F.; Liu, D.-W.; Xue, B.; Lyu, J.; Liu, J.-J.; Li, F.; Ren, X.; Ge, W.; Liu, B.; Ma, X.-L.; et al. Design and ground verification for Multispectral Camera on the Mars Tianwen-1 Rover. *Space Sci. Rev.* **2022**, *218*, 19. [CrossRef]
137. Li, B.; Yue, Z.; Qu, S.; Yao, P.; Fu, X.; Ling, Z.; Chen, S. Spatio-Temporal Analysis of Dust Storm Activity in Chryse Planitia Using MGS-MOC Observations from Mars Years 24–28. *Universe* **2021**, *7*, 433. [CrossRef]
138. Guha, B.K.; Gebhardt, C.; Young, R.M.B.; Wolff, M.J.; Montabone, L. Seasonal and diurnal variations of dust storms in Martian year 36 based on the EMM-EXI database. *J. Geophys. Res. Planets* **2024**, *129*, e2023JE008156. [CrossRef]
139. Wang, H.; Ingersoll, A.P. Martian clouds observed by Mars Global Surveyor Mars Orbiter Camera. *J. Geophys. Res.* **2002**, *107*, 5078. [CrossRef]
140. Battalio, M.; Wang, H. The Mars Dust Activity Database (MDAD): A comprehensive statistical study of dust storm sequences. *Icarus* **2021**, *354*, 114059. [CrossRef]

141. Wu, B.; Dong, J.; Wang, Y.; Rao, W.; Sun, Z.Z.; Li, Z.; Tan, Z.; Chen, Z.; Wang, C.; Liu, W.C.; et al. Landing Site Selection and Characterization of Tianwen-1 (Zhurong Rover) on Mars. *J. Geophys. Res. Planets* **2022**, *127*, e2021JE007137. [CrossRef]
142. Shirley, J.H.; McConnochie, T.H.; Kass, D.M.; Kleinböhl, A.; Schofield, J.T.; Heavens, N.G.; McCleese, D.J.; Benson, J.; Hinson, D.P.; Bandfield, J.L. Temperature and aerosol opacities of the Mars atmosphere at aphelion: Validation and inter-comparison of limb sounding profiles from MRO/MCS and MGS/TES. *Icarus* **2015**, *251*, 26–49. [CrossRef]
143. Laseigneur, Y.; Vincendon, M. OMEGA/Mars Express: A new Martian atmospheric dust hunter. *Icarus* **2023**, *392*, 115366. [CrossRef]
144. Smith, M.D.; Pearl, J.C.; Conrath, B.J.; Christensen, P.R. Mars Global Surveyor Thermal Emission Spectrometer (TES) observations of dust opacity during aerobraking and science phasing. *J. Geophys. Res.* **2000**, *105*, 9539–9552. [CrossRef]
145. Smith, M.D.; Bandfield, J.L.; Christensen, P.R.; Richardson, M.I. Thermal Emission Imaging System (THEMIS) infrared observations of atmospheric dust and water ice cloud optical depth. *J. Geophys. Res.* **2003**, *108*, 5115. [CrossRef]
146. Smith, M.D. Interannual variability in TES atmospheric observations of Mars during 1999-2003. *Icarus* **2004**, *167*, 148–165. [CrossRef]
147. Kleinböhl, A.; Schofield, J.T.; Kass, D.M.; Abdou, W.A.; Backus, C.R.; Sen, B.; Shirley, J.H.; Lawson, W.G.; Richardson, M.I.; Taylor, F.W.; et al. Mars Climate Sounder limb profile retrieval of atmospheric temperature, pressure and dust and water ice opacity. *J. Geophys. Res.* **2009**, *114*, E10006. [CrossRef]
148. Millour, E.; Forget, F.; Spiga, A.; Navarro, T.; Madeleine, J.B.; Montabone, L.; Pottier, A.; Lefevre, F.; Montmessin, F.; Chaufray, J.-Y.; et al. The Mars Climate Database (MCD version 5.2). In Proceedings of the European Planetary Science Congress 2015, Nantes, France, 27 September 2015.
149. Kleinböhl, A.; Spiga, A.; Kass, D.M.; Shirley, J.H.; Millour, E.; Montabone, L.; Forget, F. Diurnal variations of dust during the 2018 global dust storm observed by the Mars Climate Sounder. *J. Geophys. Res. Planets* **2020**, *125*, e2019JE006115. [CrossRef]
150. Vandaele, A.C.; Korablev, O.; Daerden, F.; Aoki, S.; Thomas, I.R.; Altieri, F.; López-Valverde, M.; Villanueva, G.; Liuzzi, G.; Smith, M.D.; et al. Martian dust storm impact on atmospheric H_2O and D/H observed by ExoMars Trace Gas Orbiter. *Nature* **2019**, *568*, 521–525. [CrossRef]
151. Information Office of the State Council of the People's Republic of China. *China's Spaceflight in 2021*; People's Publishing House: Beijing, China, 2022. (In Chinese)
152. Kleinböhl, A.; Schofield, J.T.; Abdou, W.A.; Irwin, P.G.J.; de Kok, R.J. A single-scattering approximation for infrared radiative transfer in limb geometry in the Martian atmosphere. *J. Quant. Spectrosc. Radiat. Transfer.* **2011**, *112*, 1568–1580. [CrossRef]
153. He, F.; Wei, Y.; Rong, Z.; Reng, Z.; Yan, L.; Tan, N.; Wang, Y.; Fan, K.; Zhou, X.; Gao, J. Monitoring methods for Martian dust storms. *Chin. Sci. Bull.* **2023**, *68*, 2046–2057. (In Chinese) [CrossRef]
154. Montabone, L.; Forget, F. On forecasting dust storms on Mars. In Proceedings of the 48th International Conference on Environmental Systems, Albuquerque, NM, USA, 8–12 July 2018.
155. Fan, K.; Wei, Y. Prospection of multi-spacecraft planetary exploration missions in upcoming future. *Chin. Sci. Bull.* **2021**, *66*, 4350–4353. (In Chinese) [CrossRef]